Advanced Functional Materials

ADVANCED FUNCTIONAL MATERIALS
www.afm-journal.de

RESEARCH ARTICLE OPEN ACCESS

Microenvironmental Reprogramming by 3D Anisotropic Cardiac Extracellular Matrix Induces Nuclear Remodeling and Epigenetic Maturation of Chemically Induced Cardiomyocytes

Seung Ju Seo[1,2] | Mi Jeong Lee[3] | Hyun Wook Kang[4] | Seonhee Byeon[1] | Soo-Kyoung Choi[1] | Nakwon Choi[5,6,7,8,9] | Seung-Woo Cho[3,10] | Yoonhee Jin[1,2]

[1]Department of Physiology, Yonsei University College of Medicine, Seoul, Republic of Korea | [2]Graduate School of Medical Science, Brain Korea 21 Project, Yonsei University College of Medicine, Seoul, Republic of Korea | [3]Department of Biotechnology, Yonsei University, Seoul, Republic of Korea | [4]School of Mechanical Engineering, Korea University, Seoul, Republic of Korea | [5]Department of Biomedical Sciences, College of Medicine, Korea University, Seoul, Republic of Korea | [6]Department of Convergence Medicine, College of Medicine, Korea University, Seoul, Republic of Korea | [7]Institute of Human Genetics, College of Medicine, Korea University, Seoul, Republic of Korea | [8]Research Institute for Convergence Biomedical Science, College of Medicine, Korea University, Seoul, Republic of Korea | [9]Bio-Medical Research Center, Korea University Guro Hospital, Seoul, Republic of Korea | [10]Center for Nanomedicine, Institute for Basic Science (IBS), Seoul, Republic of Korea

Correspondence: Nakwon Choi (nakwonchoi@korea.ac.kr) | Seung-Woo Cho (seungwoocho@yonsei.ac.kr) | Yoonhee Jin (yoonheejin@yuhs.ac)

Received: 26 November 2025 | **Revised:** 3 March 2026 | **Accepted:** 5 March 2026

Keywords: 3D anisotropy | chromatin remodeling | direct cardiac reprogramming | heart-derived extracellular matrix | nuclear mechanotransduction

ABSTRACT

Extracellular matrix (ECM) of the heart exhibits highly organized anisotropy, which is essential for directing cellular alignment, force transmission, and tissue function. However, mechanistic pathways linking ECM alignment to nuclear and epigenetic remodeling remain poorly defined, especially in the context of direct cardiac reprogramming. Here, a 3D anisotropically aligned decellularized heart ECM (HEM) is engineered to investigate how structural and biochemical cues modulate maturation of chemically induced cardiomyocyte-like cells (CiCMs). The alignment of HEM enhances cytoskeletal organization and perinuclear actin assembly, leading to nuclear elongation and intermembrane redistribution of emerin from the inner to the outer nuclear membrane. These changes are accompanied by upregulation of SUN1/2, key components of the LINC complex, and by a transient increase in nuclear YAP/TAZ localization. Chromatin condensation is reduced under aligned conditions, with corresponding increases in H3K4me3 and decreases in H3K9me3, indicative of a more transcriptionally permissive chromatin state. Functionally, CiCMs in aligned HEM exhibit improved sarcomere structure and t-tubule development, enhanced responsiveness to β-adrenergic and muscarinic stimulation, and increased contractile force under electrical pacing. These findings reveal a mechanotransductive cascade linking cardiac ECM alignment to nuclear and chromatin remodeling, ultimately promoting functional maturation of reprogrammed cardiomyocytes in a biomimetic 3D microenvironment.

1 | Introduction

The highly organized, anisotropic structure of cardiac muscle is vital for coordinating contractile activity through tight intercellular coupling, electrical signal propagation, and mechanical coupling. This aligned architecture not only reflects the morphological arrangement of cardiomyocytes but also directly influences their response to physical tension and subsequent functional maturation [1, 2]. Therefore, reconstructing a biomimetic 3D cardiac model that recapitulates this anisotropic organization is essential for regenerative therapies and physiologically relevant disease models [3, 4].

Among various strategies for generating cardiomyocytes, chemically induced cardiomyocyte-like cells (CiCMs) derived from direct reprogramming have emerged as a promising cell source, circumventing the risks associated with transgene delivery [5, 6]. However, CiCMs still exhibit immature phenotypes, with deficiencies in structural organization and contractile function, thereby necessitating further bioengineering strategies to enhance their maturation [7–10]. Recent efforts have focused on engineering biomimetic environments that provide the biochemical and biophysical cues of the native cardiac extracellular matrix (ECM). Decellularized heart ECM-derived hydrogels offer a supportive microenvironment rich in matrix proteins, including laminin, fibronectin, and various collagens, which are essential for cardiomyocyte development [6, 11]. Moreover, introducing 3D anisotropy into these ECM hydrogels has been shown to improve cellular organization and promote the structural maturation of cardiomyocytes [12–16].

While these studies underscore the significance of biophysical guidance, the mechanisms by which ECM anisotropy regulates nuclear mechanics and epigenetic remodeling in CiCMs remain largely unclear. Given that anisotropic alignment represents a directional biophysical cue, it may transmit cytoskeletal forces to the nucleus through a mechanotransductive axis that links the cytoskeleton to chromatin via the linker of nucleoskeleton and cytoskeleton (LINC) complex [17, 18]. Previous studies have shown that substrate stiffness, cyclic stretch, and geometrically controlled hydrogels can modulate nuclear morphology and chromatin organization, primarily in 2D or single-cell settings [19–24]. However, these systems often rely on synthetic matrices or microfabricated patterns and do not recapitulate the topographical or compositional complexity of native cardiac ECM. Thus, it remains unclear whether ECM alignment alone–within a native, tissue-specific 3D ECM environment–is sufficient to induce nuclear remodeling and epigenetic reprogramming, particularly in the context of direct cardiac reprogramming.

In this study, we developed a 3D anisotropically aligned decellularized heart-derived ECM (HEM) system that directs CiCM alignment and recapitulates the structural and biochemical features of native cardiac tissue. We demonstrate that this aligned microenvironment promotes nuclear elongation and structural remodeling via LINC-associated components, leading to epigenetic maturation characterized by changes in H3K4me3 and H3K9me3. These nuclear and chromatin alterations strongly correlate with enhanced sarcomeric organization and contractile function of CiCMs. Together, our findings uncover a mechanistic link between ECM-guided alignment, nuclear remodeling, and epigenetic regulation that has not been characterized in the context of cardiac reprogramming, offering new insights for engineering functionally mature cardiac tissues.

2 | Results and Discussion

2.1 | 3D-Aligned HEM Promotes Perinuclear F-Actin Accumulation and Nuclear Deformation in CiCMs

To examine how ECM alignment and biochemical composition influence cytoskeletal and nuclear organization in CiCMs, we exploited a 3D hydrogel system with tunable fibrillar orientation using a strain-release mechanism [14, 25]. Four experimental conditions were generated: aligned and randomized hydrogels composed of either type I collagen (C-Align, C-Random) or HEM (H-Align, H-Random). Release of uniaxial strain, which had been applied to a PDMS chamber containing type I collagen (COL) or HEM, during the early sol–gel transition induced fibril alignment. Release timing was optimized at 5 min for COL and 8 min for HEM to coincide with partial fibrillogenesis and enable mechanical reorientation (Figure S1a–d). CiCMs were encapsulated before alignment, and viability remained high across all conditions (Figure S1e). Rheological analysis of cell-free COL and HEM hydrogels under random and aligned conditions showed higher storage moduli in COL compared with HEM matrices (Figure S2a,b). Within each hydrogel system, alignment did not significantly change bulk stiffness, indicating that fibrillar orientation did not alter the macroscopic mechanical properties.

Matrix alignment induced coordinated orientation of both F-actin filaments and nuclei along the ECM axis, whereas random matrices exhibited disorganized cytoskeletal and nuclear architecture (Figure 1a,b; Figure S3). These observations suggest that 3D topographical anisotropy provides contact guidance cues that propagate from the ECM through the cytoskeleton to the nucleus (Figure 1c) [26, 27]. To quantify force-transducing cytoskeletal remodeling, perinuclear F-actin–a structure implicated in nuclear force transmission–was examined. By day 3, both aligned groups displayed dense perinuclear actin structures, with the most substantial accumulation observed in H-Align (Figure 1d; Figure S4a,b). Quantitative analysis confirmed significantly elevated perinuclear F-actin intensity in aligned matrices compared to their random counterparts across days 1, 3, and 7, with the H-Align group consistently showing the most robust effect (Figure 1e; Figure S4c). At day 1, perinuclear F-actin intensity in H-Align was 2.02-fold greater than in C-Random, 1.53-fold higher than in C-Align, and 1.35-fold higher than in H-Random. Orthogonal confocal views revealed actin cables enveloping the nuclear periphery along the central axis, consistent with perinuclear actin cap formation [28, 29].

Analysis of nuclear morphology further demonstrated that aligned matrices decreased nuclear circularity and increased nuclear area–both indicators of nuclear elongation–starting from day 1 (Figure 1f,g; Figure S4d,e). Among all groups, H-Align exhibited the most pronounced nuclear deformation, with circularity values that were 16.1%, 20.9%, and 27.5% lower than C-Random at days 1, 3, and 7, respectively. Within each ECM

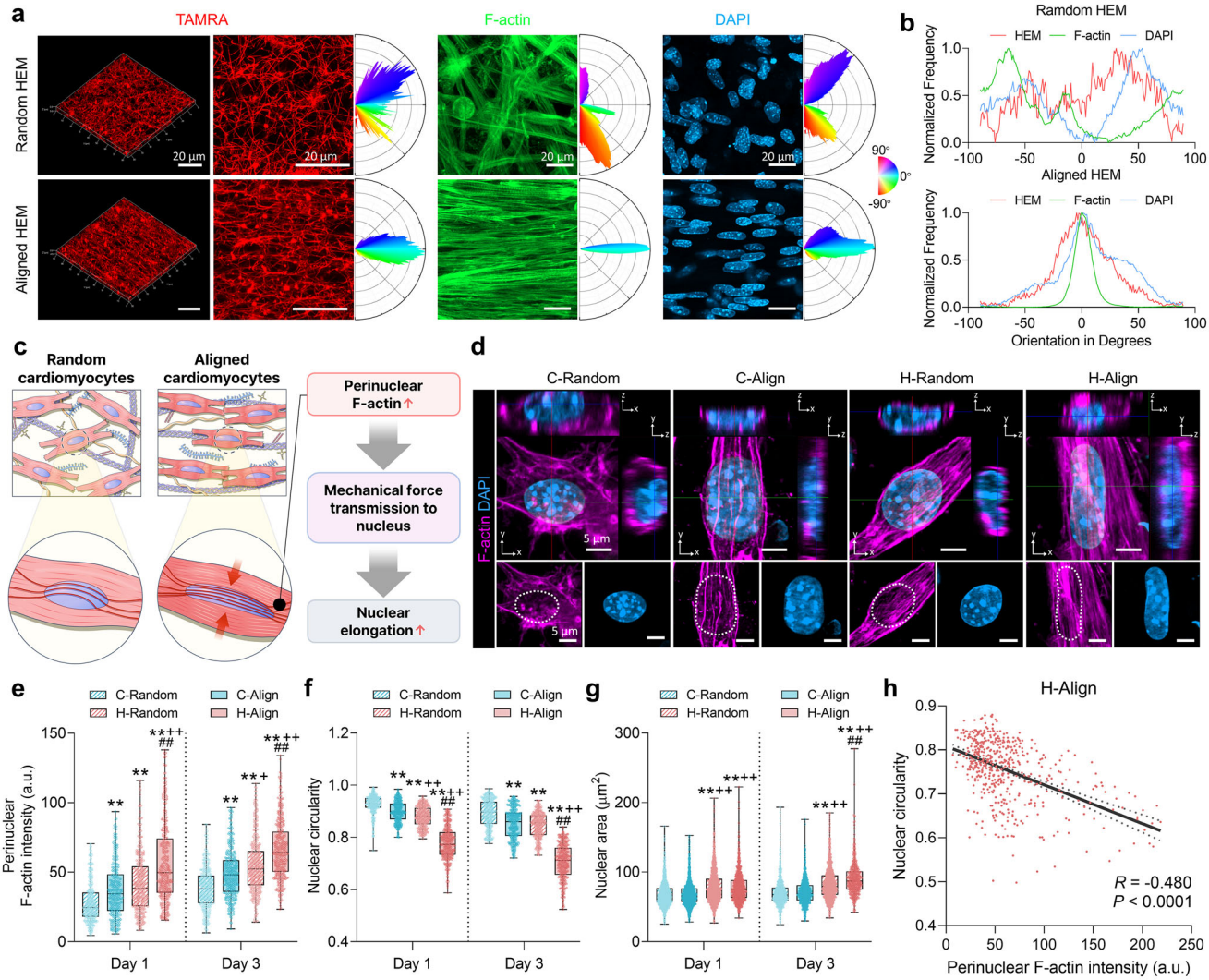

FIGURE 1 | 3D HEM alignment directs cytoskeletal and nuclear orientation and modulates perinuclear actin organization of CiCMs. (a) Representative 3D confocal images of 5(6)-TAMRA-SE–labeled ECM microfibrils (red, acellular) in randomly oriented (top) and aligned (bottom) HEM hydrogels. Middle and right panels show F-actin (green) and nuclei (DAPI, blue) in encapsulated CiCMs. Orientation histograms (right) depict angular distributions from −90° to +90° (scale bars = 20 μm). (b) Normalized angular histograms corresponding to (a). (c) Schematic illustration showing that ECM alignment enhances perinuclear F-actin assembly, promoting nuclear elongation via force transmission. (d) Cross-sectional images of CiCMs at day 3 in C-Random, C-Align, H-Random, and H-Align groups, showing F-actin (magenta) and nuclei (DAPI, blue). White dashed circles highlight nuclear boundaries (scale bars = 5 μm). Quantification of (e) perinuclear F-actin intensity (n = 325–386), (f) nuclear circularity (n = 383), and (g) nuclear area (n = 497–1443) at day 1 and day 3. Circularity index = 1.0 represents a perfect circle. Statistical significance was determined by one-way ANOVA followed by Tukey's multiple comparisons test (**$p < 0.01$ vs. C-Random; $^{+}p < 0.05$, $^{++}p < 0.01$ vs. C-Align; $^{\#\#}p < 0.01$ vs. H-Random). Data are shown as mean ± SD. (h) Correlation between perinuclear F-actin intensity and nuclear circularity in H-Align at day 3, assessed using two-tailed Pearson's correlation analysis (Pearson's $R = -0.480$, $p < 0.0001$, $n = 518$).

type, alignment had a more substantial effect in HEM than in COL: at day 3, nuclear circularity was reduced by 4.4% in C-Align compared to C-Random, whereas the reduction reached 16.7% in H-Align compared to H-Random. Nuclear area followed a similar trend, increasing significantly in aligned matrices and peaking in H-Align.

To explore whether these morphological changes were driven by cytoskeletal tension, perinuclear F-actin intensity was correlated with nuclear circularity (Figure 1h; Figure S4f). In the correlation analysis, a negative R value indicates that lower nuclear circularity–meaning a more elongated nucleus– is associated with higher perinuclear F-actin intensity, reflecting the tendency of elevated cytoskeletal tension to induce nuclear deformation. In HEM matrices, higher perinuclear F-actin levels were significantly associated with nuclear elongation, particularly in H-Align ($R = -0.480$). This relationship was not observed in COL groups, suggesting that the biochemical complexity of HEM synergizes with its anisotropic structure to enhance force transmission to the nucleus. Together, these results suggest that 3D matrix anisotropy serves as a structural template that is sequentially coupled to cytoskeletal alignment and nuclear reshaping, which are key events in the mechanotransductive processes [30, 31].

2.2 | Aligned HEM Alters Nuclear Envelope Composition via Emerin Redistribution and Enhanced SUN1/2 Regulation

While nuclear elongation has been linked to changes in mechanical load, how such deformation influences the composition and organization of the nuclear envelope remains incompletely understood. To address this, we examined the distribution of mechanotransductive nuclear membrane proteins in response to ECM alignment. Among these, emerin and the SUN-domain family (SUN1 and SUN2) are central regulators of cytoskeletal-nuclear coupling. Emerin, predominantly localized at the inner nuclear membrane (INM), mediates interactions with lamins and the cytoskeleton and plays a critical role in transmitting mechanical signals across the nuclear envelope [32, 33]. Under mechanical strain, emerin undergoes redistribution between membranes in coordination with actomyosin remodeling and chromatin reorganization [32, 34]. SUN1 and SUN2, core components of the LINC complex, span the inner nuclear membrane and connect cytoplasmic nesprins to the nuclear lamina, enabling load transfer to the nuclear interior [18, 35].

Alignment-induced nuclear deformation in HEM is accompanied by a marked translocation of emerin from the INM to the outer nuclear membrane (ONM), along with an increased SUN1/2 expression, indicating enhanced nuclear-cytoskeletal coupling (Figure 2a). To visualize emerin localization in a nuclear membrane-specific manner, digitonin was used to selectively permeabilize the ONM, while Triton X-100 was used to access both membranes (Figure 2b; Figure S5a,b). Lamin A/C staining under INM-access conditions was used to validate nuclear membrane specificity [31, 34].

At day 3, ONM-localized emerin was significantly elevated in aligned conditions, with the H-Align group showing the highest signal intensity (Figure 2c). Compared to C-Random, ONM emerin increased by 8.67% in C-Aligned and by 84.05% in H-Align relative to H-Random. (Figure 2c). In contrast, INM-localized emerin was diminished in aligned matrices, with the lowest levels observed in H-Align–28.55% lower than H-Random, and 28.83% lower than C-Align (Figure 2d). These opposing shifts suggest a redistribution of emerin from the INM to the ONM in response to ECM alignment. A temporal analysis from day 1 to day 7 confirmed this pattern (Figure S5a–d). ONM-associated emerin remained elevated in aligned groups through day 7, while the INM reduction partially recovered by day 7, with only a modest difference between H-Align and H-Random (3.36%). These kinetics suggest that emerin redistribution peaks around day 3 and partially resolves over time.

A correlation was observed between nuclear envelope remodeling and nuclear deformation. Specifically, higher ONM-localized emerin intensity was associated with more elongated nuclei, whereas higher INM-localized emerin correlated with more circular nuclei at day 3 (Figure 2e,f; Figure S5e,f). These trends support a model in which nuclear elongation is accompanied by a redistribution of emerin from the inner to the outer nuclear membrane.

To assess whether this nuclear remodeling is accompanied by changes in key components of the LINC complex, SUN1 and SUN2 levels were quantified by Western blot. At day 3, both SUN1 and SUN2 were elevated under aligned conditions, with the highest expression observed in H-Align (Figure 2g,h; Figure S6). SUN1 expression increased by 1.57-fold in C-Align, 1.44-fold in H-Random, and 1.95-fold in H-Align relative to C-Random. Similarly, SUN2 expressions increased by 1.46-fold, 1.48-fold, and 1.75-fold, respectively. These findings indicate that structural alignment in tissue-specific matrix is associated with nuclear envelope remodeling in CiCMs, characterized by emerin translocation from the INM to the ONM and increased SUN1/2 expression. These changes proceed in parallel with nuclear elongation and likely reinforce mechanical coupling across the cytoskeletal-nuclear axis, a configuration associated with mechanosignaling linked to chromatin reconfiguration and transcriptional activation [23, 36, 37].

2.3 | 3D HEM Anisotropy Induces Transient YAP Activation and Nuclear Epigenetic Remodeling in CiCMs

How mechanical deformation at the nuclear envelope influences transcriptional activation and chromatin remodeling remains incompletely understood. To investigate whether ECM alignment activates mechanosensitive transcriptional pathways, we assessed the localization and gene expression of Yes-associated protein (YAP) and PDZ-binding motif (TAZ), as well as histone modification changes in CiCMs. YAP and TAZ are transcriptional co-activators regulated by the Hippo pathway that translocate to the nucleus in response to mechanical cues, initiating gene expression programs [38].

Under aligned conditions, nuclear-to-cytoplasmic YAP ratios increased transiently, peaking at days 1 and 3 and returning to baseline by day 7 (Figure 3a,b; Figure S7a,b). This was accompanied by significantly elevated mRNA levels of *Yap1* and *Wwtr1* (encoding TAZ) in H-Align compared to H-Random at day 3 (Figure 3c). These temporal dynamics coincided with peak nuclear elongation and LINC remodeling, suggesting that transient mechanical input from ECM anisotropy activates YAP/TAZ signaling [39]. This pattern is consistent with prior findings in early cardiomyocyte differentiation, in which YAP/TAZ activity is known to diminish as cells progress toward a mature state [40].

Chromatin architecture was significantly remodeled in response to ECM alignment, indicative of a shift toward a more transcriptionally permissive state (Figure 3d). Chromatin condensation parameters (CCP), calculated from DAPI intensity texture analysis using Sobel edge detection, were markedly reduced in aligned groups at days 3 and 7, reflecting chromatin decondensation (Figure 3e; Figure S8) [41]. Among all groups, H-Align exhibited the most pronounced reduction–43.5% at day 3 and 41.1% at day 7–compared to H-Random. In contrast, C-Align showed a more modest decrease of 32.6% and 26.3% relative to C-Random at corresponding time points. These data indicate that 3D ECM alignment is associated sustained chromatin relaxation, particularly in the presence of cardiac-specific biochemical

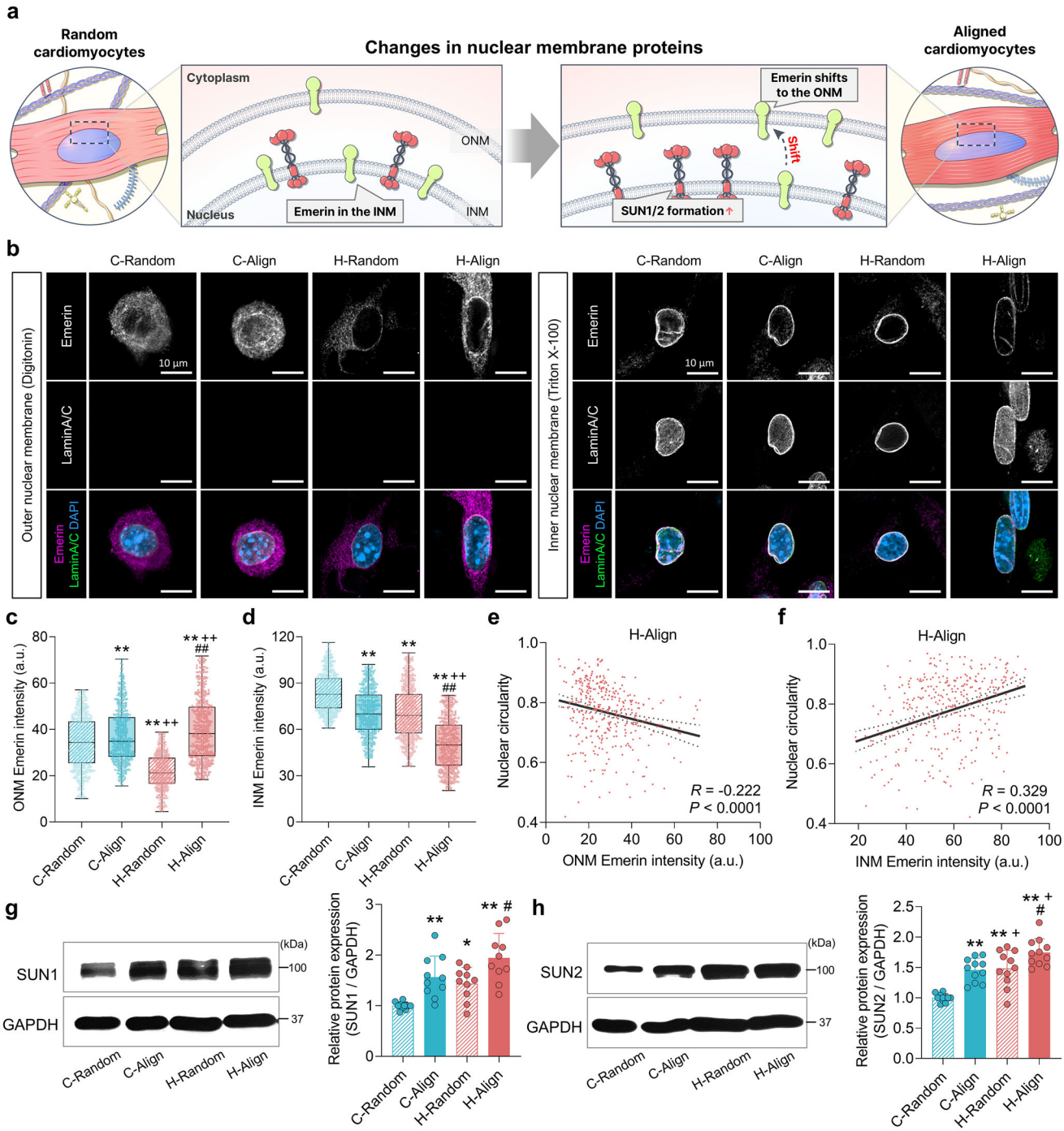

FIGURE 2 | HEM alignment alters nuclear membrane protein distribution in CiCMs. (a) Schematic showing alignment-induced changes in nuclear membrane organization. ECM alignment promotes nuclear elongation, accompanied by redistribution of emerin and modulation of SUN1/2 expression. (b) Immunofluorescence images of CiCMs at day 3 in C-Random, C-Align, H-Random, and H-Align. Digitonin permeabilization (left) reveals emerin localized on the outer nuclear membrane (ONM), verified by weak Lamin A/C staining. Triton X-100 permeabilization (right) allows detection of emerin on the inner nuclear membrane (INM), where Lamin A/C is detected (scale bars = 10 μm). (c,d) Quantification of emerin intensity at the nuclear envelope on day 3. Box plots show the intensity of emerin localized at the (c) ONM (n = 466–534) and the (d) INM (n = 471–556). (e,f) Correlation of emerin localization with nuclear geometry in the H-Align group. Scatter plots show the correlation between nuclear circularity and (e) ONM emerin intensity (n = 379), and (f) INM emerin intensity (n = 338), assessed using two-tailed Pearson's correlation analysis (e: Pearson's $R = -0.222$, $p < 0.0001$; f: Pearson's $R = 0.329$, $p < 0.0001$). (g) Western blot analysis of SUN1 expression at day 3 and quantification relative to the C-Random group (n = 10). (h) Western blot analysis of SUN2 expression at day 3 and quantification relative to the C-Random group (n = 11). Protein expression was normalized to GAPDH. Statistical significance was determined by one-way ANOVA followed by Tukey's multiple comparisons test (*$p < 0.05$, **$p < 0.01$ vs. C-Random; $^{+}p < 0.05$, $^{++}p < 0.01$ vs. C-Align; $^{\#}p < 0.05$, $^{\#\#}p < 0.01$ vs. H-Random). All data are expressed as mean ± SD.

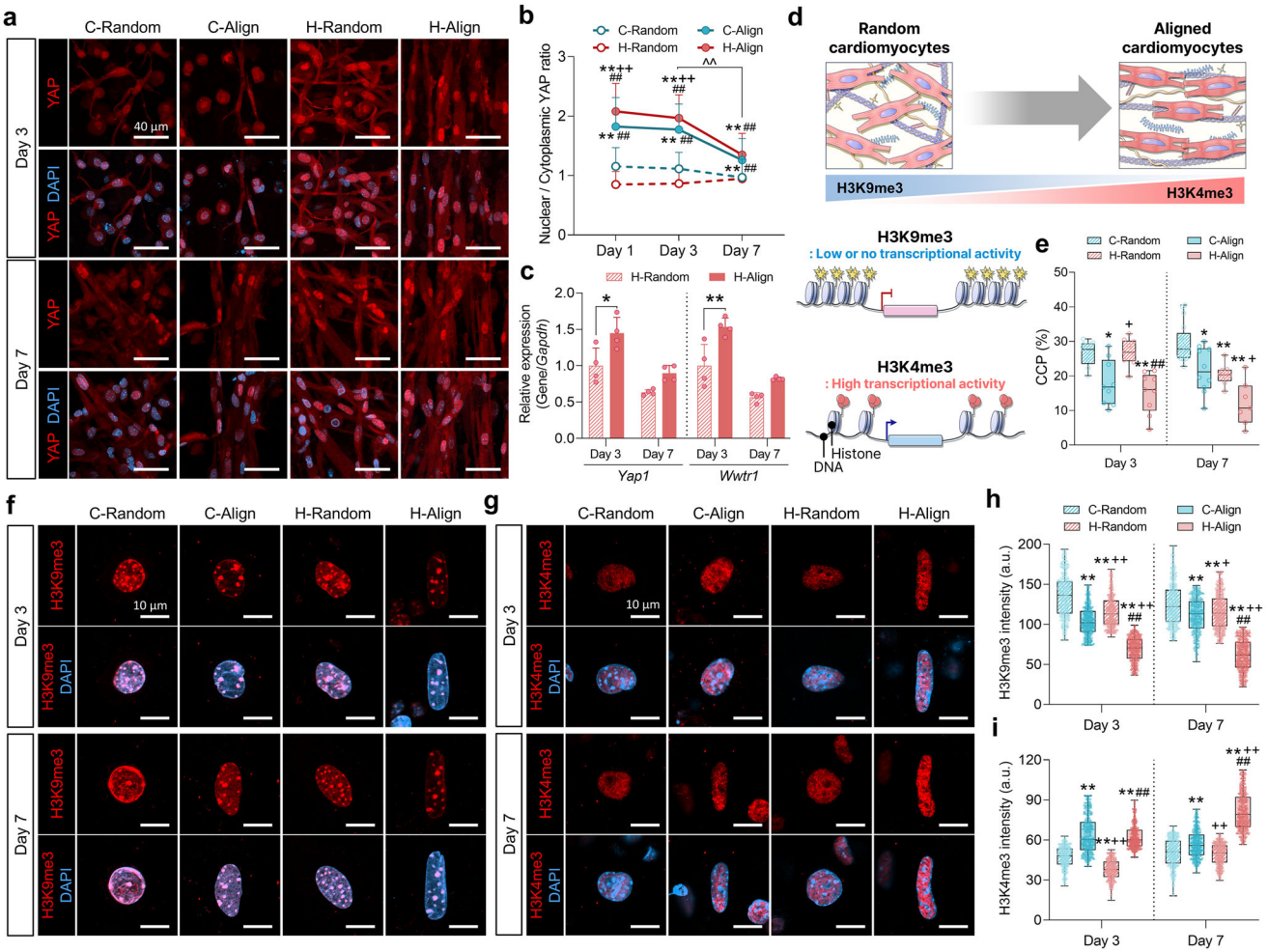

FIGURE 3 | 3D-aligned HEM promotes transcriptional activity through YAP signaling and histone modification in CiCMs. (a) Immunofluorescence images of CiCMs cultured in C-Random, C-Align, H-Random, and H-Align conditions on day 3 and 7, stained for YAP (red) and nuclei (DAPI, blue) (scale bars = 40 μm). (b) Quantification of the nuclear-to-cytoplasmic YAP ratio (n = 192–232). Statistical significance was assessed using two-way ANOVA followed by Tukey's multiple comparisons test (**$p < 0.01$ vs. C-Random; $^{++}p < 0.01$ vs. C-Align; $^{\#\#}p < 0.01$ vs. H-Random; $\hat{}\hat{}p < 0.01$ for day 3 vs. day 7 in align groups). (c) Quantitative RT-PCR analysis of *Yap1* and *Wwtr1* (*Taz*) mRNA expression in H-Random and H-Align groups at days 3 and 7 (n = 4; two-way ANOVA followed by Tukey's multiple comparisons test, *$p < 0.05$, **$p < 0.01$ vs. H-Random). (d) Schematic illustrations of chromatin state transitions from transcriptionally repressive (H3K9me3-enriched) to active (H3K4me3-enriched). (e) Chromatin condensation parameters (CCP), defined as the proportion of condensed chromatin area within the nucleus, measured from DAPI images (n = 7–17; one-way ANOVA followed by Tukey's multiple comparisons test, *$p < 0.05$, **$p < 0.01$ vs. C-Random; $^{+}p < 0.05$ vs. C-Align; $^{\#\#}p < 0.01$ vs. H-Random). (f,g) Representative single-nucleus images of CiCMs showing the expression of (f) H3K9me3 and (g) H3K4me3 on day 3 and 7 (scale bars = 10 μm). (h,i) Quantification of the fluorescence intensity for (h) H3K9me3 (n = 299–396) and (i) H3K4me3 (n = 341–388) on day 3 and day 7. Statistical significance was determined by one-way ANOVA followed by Tukey's multiple comparisons test (**$p < 0.01$ vs. C-Random; $^{+}p < 0.05$, $^{++}p < 0.01$ vs. C-Align; $^{\#\#}p < 0.01$ vs. H-Random). All data are expressed as mean ± SD.

cues. This decompacted chromatin state is associated with increased chromatin availability, transcription factor accessibility, and increased nuclear mechanical flexibility, which directly correlates with improved initial reprogramming efficiency [42, 43]. The observed sustained reduction in CCP within aligned HEM thus suggests a transition toward an open chromatin configuration that may facilitate activation of the cardiac gene program.

This chromatin relaxation was further supported by changes in histone methylation marks associated with transcriptional activity. Trimethylation of histone H3 lysine 9 (H3K9me3), a marker of transcriptionally repressive heterochromatin, was consistently reduced in aligned conditions across all time points, with H-Align showing the lowest levels (Figure 3f,h; Figure S7c,d). Conversely, H3K4me3 levels, a hallmark of active euchromatin, increased with alignment, peaking in H-Align at day 7, where levels were 1.65-fold higher than H-Random and 1.43-fold higher than C-Align (Figure 3g,i; Figure S7e,f). These opposing shifts in histone methylation states coincide with the reduction in CCP and further indicate a transition toward a more transcriptionally permissive chromatin state [43, 44]. 3D ECM anisotropy, coupled with heart-specific biochemical cues, elicits a transient mechanosensitive response and promotes epigenetic remodeling, supporting an association between matrix architecture and transcriptional regulation.

2.4 | Cytoskeletal Tension and SUN1/2 Coupling Contribute to Alignment-Associated Nuclear and Chromatin Remodeling

The role of cytoskeletal tension and nucleus-cytoskeleton coupling in alignment-associated nuclear and chromatin remodeling was functionally evaluated using targeted modulation. Actomyosin contractility was transiently inhibited during the early mechanosensing window using the Rho-associated protein kinase (ROCK) inhibitor Y-27632, and SUN1/2-mediated LINC coupling was reduced via siRNA knockdown.

ROCK inhibition markedly reduced perinuclear F-actin accumulation in both H-Random and H-Align matrices, with a more pronounced reduction under aligned conditions (Figure 4a,b). Nuclear circularity in H-Align increased from 0.74 ± 0.08 to 0.92 ± 0.03 following ROCK inhibition, reaching levels comparable to H-Random. In contrast, nuclear circularity in H-Random exhibited only a modest change (0.89 ± 0.05 in NT vs. 0.92 ± 0.03 in Y-27632-treated cells), suggesting that alignment-associated nuclear elongation may be more responsive to ROCK-dependent contractility (Figure 4a,c). Elevated nuclear-to-cytoplasmic YAP ratios observed under H-Align were significantly reduced following ROCK inhibition, approaching levels observed in H-Random (Figure 4d,e). In contrast, YAP distribution in H-Random showed no significant change upon ROCK inhibition. H3K4me3 intensity decreased and H3K9me3 intensity increased following ROCK inhibition in both matrix conditions, with a greater shift observed in H-Align compared to H-Random (Figure 4f,g).

To further examine the role of force transmission across the nuclear envelope, nucleus–cytoskeleton coupling was reduced by siRNA-mediated knockdown of *Sun1* and *Sun2*, core components of the LINC complex (Figure 4h–l; Figure S9). In the double-knockdown (siSun1/2) group, *Sun1* and *Sun2* expression levels were decreased by 45.5% and 63.0%, respectively, relative to non-targeting controls (Figure S9a). Perinuclear F-actin organization and nuclear elongation were largely preserved following *Sun1/2* knockdown (Figure 4h,i; Figure S9b), suggesting that the observed degree of *Sun1/2* reduction was not sufficient to substantially alter cytoskeletal alignment or nuclear morphology. Nuclear-to-cytoplasmic YAP ratios showed no change in H-Random matrices and only a minimal reduction in H-Align following *Sun1/2* knockdown (Figure 4j; Figure S9c), suggesting that either alignment-associated YAP nuclear localization is not solely dependent on SUN1/2-mediated coupling or that more complete depletion may be required to reveal its full contribution. In contrast, chromatin-related readouts were significantly affected under aligned conditions. In H-Aligned, H3K4me3 intensity decreased from 63.1 ± 14.1 a.u. to 44.2 ± 12.9 a.u., approaching levels observed in H-Random (40.2 ± 10.6 to 41.6 ± 12.8 a.u.). H3K9me3 intensity increased from 75.1 ± 32.1 a.u. to 107.5 ± 31.3 a.u., although remaining lower than levels in H-Random controls (135.1 ± 33.6 to 147.0 ± 38.1 a.u.) (Figure 4k,l; Figure S9d).

Together, these findings indicate that actomyosin-dependent tension is closely linked to alignment-associated nuclear deformation and chromatin remodeling. Furthermore, *Sun1/2* knockdown significantly altered histone modification profiles under aligned conditions. Although additional pathways may also contribute, these observations are consistent with mechanotransductive coupling between ECM architecture and chromatin state regulation.

2.5 | 3D-Aligned HEM Accelerates Structural and Metabolic Maturation of CiCMs

Building on the established mechanotransductive axis, we evaluated whether the aligned 3D HEM microenvironment promotes maturation of CiCMs at day 7. Immunostaining for α-actinin and cardiac troponin T (cTnT) revealed more distinct sarcomere organization with well-aligned myofibrils under aligned conditions, most prominently in the H-Align group (Figure 5a). Specifically, orientation index (OI) analysis demonstrated that H-Align (OI = 0.77) achieved a substantially greater myofibrillar alignment compared to C-Align (OI = 0.61) (Figure 5b). Furthermore, the α-actinin- and cTnT-positive areas were increased in HEM conditions compared with COL groups, with H-Align exhibiting the highest coverage (Figure 5c,d).

Gene expression analysis further supported enhanced cardiac differentiation and metabolic progression. Among cardiac-related genes, the early cardiac transcription factors, *Nkx2-5* and *Mef2c*, were expressed at higher levels in HEM groups than in COL groups, with the greatest increase in H-Align (Figure 5e) [45, 46]. The mature contractile isoform *Myh7* expression also reached its highest level in H-Align [1]. Metabolism-related genes associated with fatty acid oxidation, including *Cpt1b* and *Ppara*, as well as mitochondrial biogenesis factor, *Tfam*, were similarly upregulated in H-Align, indicating a shift toward oxidative metabolism (Figure 5f) [47–49]. *Nfe2l2*, a regulator of metabolic and antioxidant responses, was likewise most elevated in H-Align [50]. These gene expression profiles indicate that the anisotropic HEM environment supports transcriptional programs essential for cardiomyocyte development.

Structural characterization further substantiated CiCM maturation. Transverse tubule (t-tubule) structures visualized by wheat germ agglutinin (WGA) labeling were more prominently developed in aligned groups, particularly H-Align (Figure 5g). Sarcomere length in H-Align approached 2.2 μm, a value typically associated with mature cardiomyocytes (Figure 5h) [1]. Electrical coupling was also enhanced as connexin 43 (Cx43) polarized toward the cell termini in H-Align, accompanied by the highest Cx43-positive area (Figure 5i) [51]. However, Cx43 organization remained distinct from that of fully mature cardiomyocytes, with residual lateral membrane localization indicative of an immature gap junction pattern. Relative to primary neonatal cardiomyocytes (nCMs), CiCMs cultured in H-Align exhibited elevated expression of the early cardiac transcription factor *Mef2c*, while functional and metabolic genes (*Nkx2-5*, *Myh7*, *Scn5a*, *Cpt1b*, and *Ppara*) were largely comparable to nCM levels (Figure S10). In contrast, *Gja1* expression reached only ~39.5% of nCM levels, indicating incomplete maturation of intercellular electrical coupling. These observations are consistent with prior reports in 3D human induced pluripotent stem cell-derived cardiomyocyte systems, in which 3D tissue organization alone typically results in fetal- or intermediate-like phenotypes [52, 53]. Further

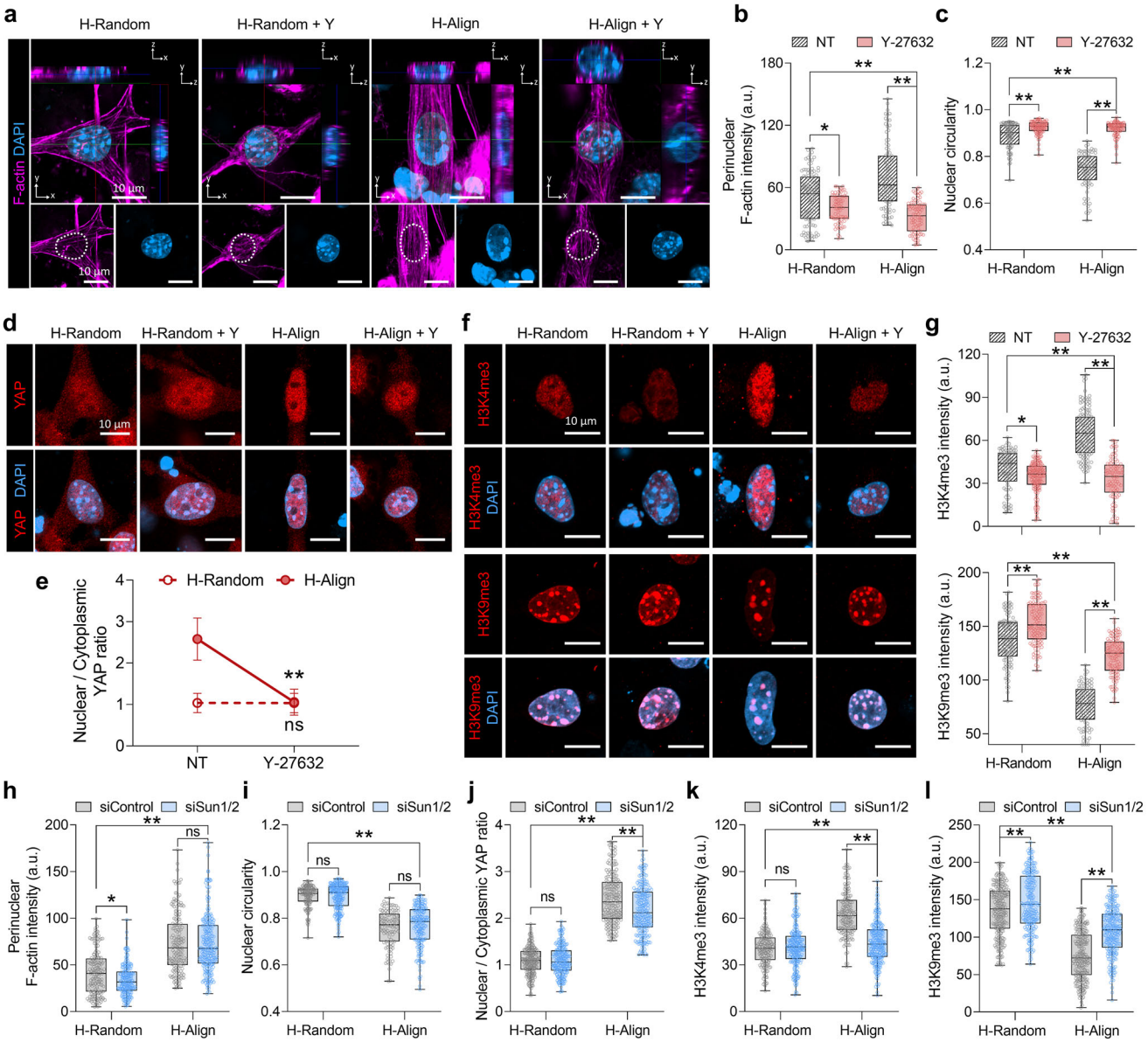

FIGURE 4 | Modulation of actomyosin tension and *Sun1/2* coupling alters alignment-dependent nuclear and chromatin organization. (a) Representative immunofluorescence images of CiCMs cultured under H-Random, H-Random + Y, H-Align, and H-Align + Y conditions, where Y indicates treatment with the ROCK inhibitor Y-27632 for 48 h, showing F-actin (magenta) and nuclei (DAPI, blue). Dashed outlines indicate nuclear boundaries (scale bars = 10 μm). (b) Quantification of perinuclear F-actin intensity (n = 74–106). (c) Quantification of nuclear circularity (n = 76–103). Circularity index = 1.0 represents a perfect circle. (d) Representative immunofluorescence images showing YAP localization (red) and nuclei (DAPI, blue) in CiCMs cultured under H-Random, H-Random + Y, H-Align, and H-Align + Y conditions (scale bars = 10 μm). (e) Quantification of the nuclear-to-cytoplasmic YAP ratio in H-Random and H-Align groups with or without Y-27632 treatment (n = 81–112; two-way ANOVA followed by Tukey's multiple comparisons test, ns; not significant, $^{**}p < 0.01$ vs. NT group). (f) Immunofluorescence images of H3K4me3 and H3K9me3 (red) with nuclear counterstaining (DAPI, blue) (scale bars = 10 μm). (g) Quantification of H3K4me3 (n = 89–157) and H3K9me3 (n = 96–116) fluorescence intensity. (h–l) Functional disruption of nuclear force transmission by siRNA-mediated knockdown of *Sun1/2*. Quantification of (h) perinuclear F-actin intensity (n = 168–248) and (i) nuclear circularity (n = 106–218). (j) Nuclear-to-cytoplasmic YAP ratio (n = 192–243). Quantification of (k) H3K4me3 (n = 171–255) and (l) H3K9me3 (n = 240–252) intensities. Statistical significance was assessed using two-way ANOVA followed by Tukey's multiple comparisons test (ns; not significant, $^{*}p < 0.05$, $^{**}p < 0.01$). All data are expressed as the mean ± SD.

maturation, including improved intercellular junction organization, has been achieved when additional external cues such as electrical stimulation are applied [52].

Collectively, these data indicate that aligned HEM promotes structural, metabolic, and transcriptional progression of CiCMs, while additional conditioning strategies may be required to achieve a more fully mature functional phenotype. The enhanced performance observed in H-Align further suggests that cardiac ECM–derived biochemical cues act synergistically with structural anisotropy to facilitate CiCM maturation beyond alignment alone.

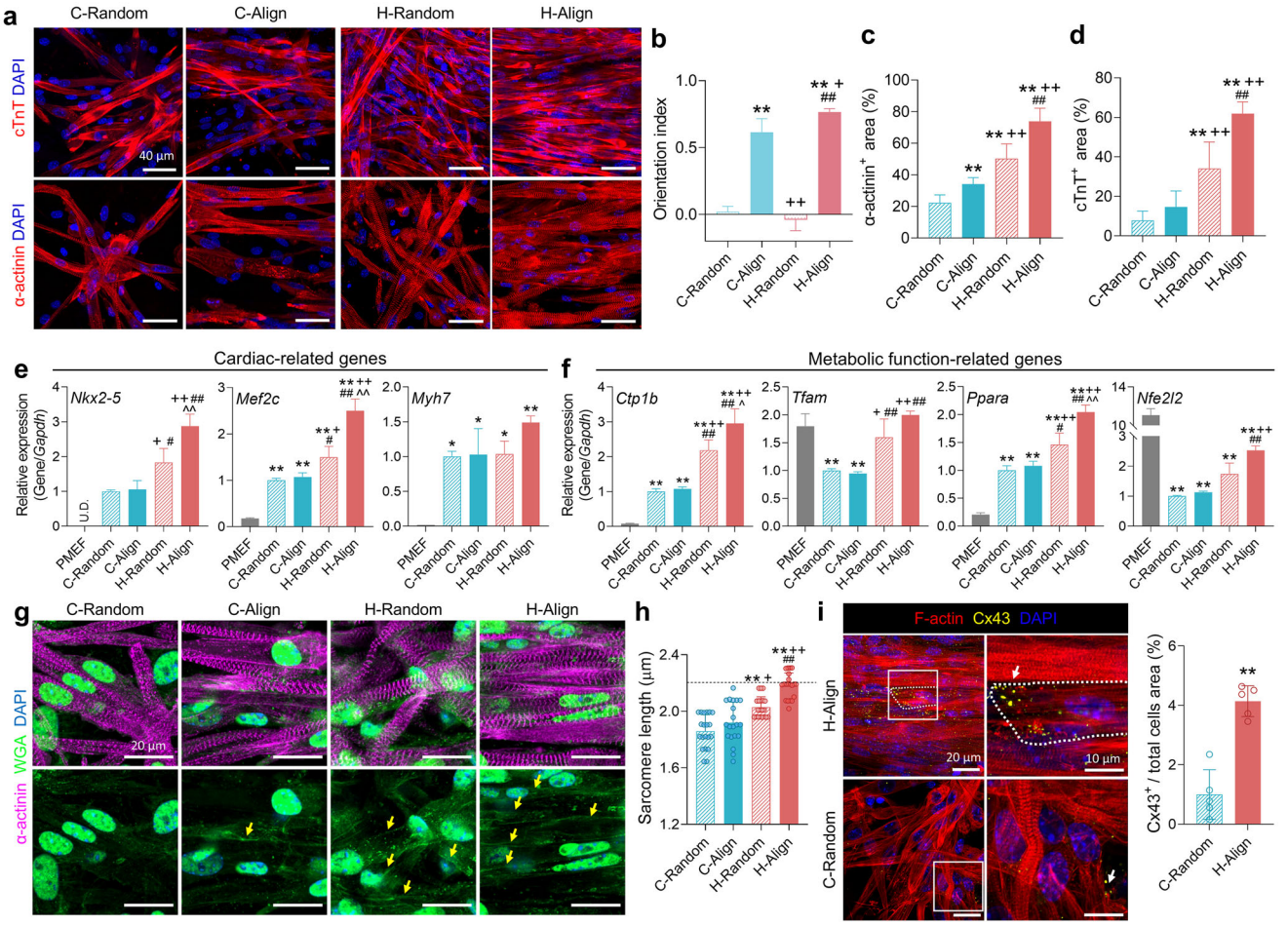

FIGURE 5 | 3D HEM alignment enhances structural and functional maturation of CiCMs. (a) Immunostaining of CiCMs for cTnT and α-actinin under C-Random, C-Align, H-Random, and H-Align (scale bars = 40 μm). (b) Orientation index of CiCMs in each hydrogel construct from the frequency distribution of orientation angles ($n = 4$; one-way ANOVA followed by Tukey's multiple comparisons test, $^{**}p < 0.01$ vs. C-Random; $^{+}p < 0.05$, $^{++}p < 0.01$ vs. C-Align; $^{\#\#}p < 0.01$ vs. H-Random). (c,d) Measurement of (c) α-actinin-positive and (d) cTnT-positive areas ($n = 10$; one-way ANOVA followed by Tukey's multiple comparisons test, $^{**}p < 0.01$ vs. C-Random; $^{++}p < 0.01$ vs. C-Align; $^{\#\#}p < 0.01$ vs. H-Random). (e,f) qRT-PCR analysis of the mRNA expression of (e) cardiac-related and (f) metabolic function-related genes ($n = 3$). For PMEFs, *Nkx2-5* was undetectable (U.D.), and *Myh7* was detected in only one replicate. Statistical significance was assessed by one-way ANOVA followed by Tukey's multiple comparisons test ($^{*}p < 0.05$, $^{**}p < 0.01$ vs. PMEF; $^{+}p < 0.05$, $^{++}p < 0.01$ vs. C-Random; $^{\#}p < 0.05$, $^{\#\#}p < 0.01$ vs. C-Align; $^{\wedge}p < 0.05$, $^{\wedge\wedge}p < 0.01$ vs. H-Random). (g) Immunofluorescence staining for α-actinin (magenta) and t-tubules (detected by WGA, green) in CiCMs (scale bars = 20 μm). Yellow arrows indicate t-tubules structures. (h) Quantification of sarcomere length in all groups ($n = 20$; one-way ANOVA followed by Tukey's multiple comparisons test, $^{**}p < 0.01$ vs. C-Random; $^{+}p < 0.05$, $^{++}p < 0.01$ vs. C-Align; $^{\#\#}p < 0.01$ vs. H-Random). (i) Immunostaining for connexin 43 (Cx43, yellow) and F-actin (red), and quantification of Cx43-positive area relative to the total cell area ($n = 5$; two-tailed unpaired Student's t-test, $^{**}p < 0.01$ vs. C-Random). All analyses were performed on day 7, and all data are presented as mean ± SD.

2.6 | 3D-Aligned HEM Enhances Electrophysiological Contractile Function of CiCMs

To evaluate the electrophysiological maturation of CiCMs in the 3D HEM anisotropy, we assessed intracellular Ca^{2+} dynamics using pharmacological responsiveness. Ca^{2+} transients were measured using the fluorescent Ca^{2+} indicator Fluo-4 AM. Isoproterenol, a β-adrenergic receptor agonist, enhances calcium influx and contractility through the cyclic AMP-protein kinase A (cAMP–PKA) pathway, whereas carbachol, a muscarinic acetylcholine receptor agonist, suppresses calcium entry and heart rate [54, 55]. Upon 10 μm isoproterenol treatment, the H-Align group maintained regular calcium transients. It exhibited a 141.96% increase in beats per minute (BPM), whereas the C-Random group showed irregular patterns and no significant increase in BPM (Figure 6a,b). Similarly, 10 μm carbachol induced stable, rhythmic BPM reductions in H-Align (47.48%), whereas the C-Random group displayed irregular traces and a 67.03% decrease in BPM (Figure 6c,d). These electrophysiological behaviors demonstrate that H-Align exhibits the most robust and physiologically appropriate responses to both β-adrenergic and muscarinic stimulation, reflecting an autonomic modulation pattern consistent with more mature cardiomyocytes [52, 56].

Next, contractile performance under electrical stimulation was evaluated. At 1 Hz pacing with 5 V, all groups contracted synchronously at 60 BPM with a consistent 1-s peak-to-peak interval. However, the contraction amplitude was markedly higher in the

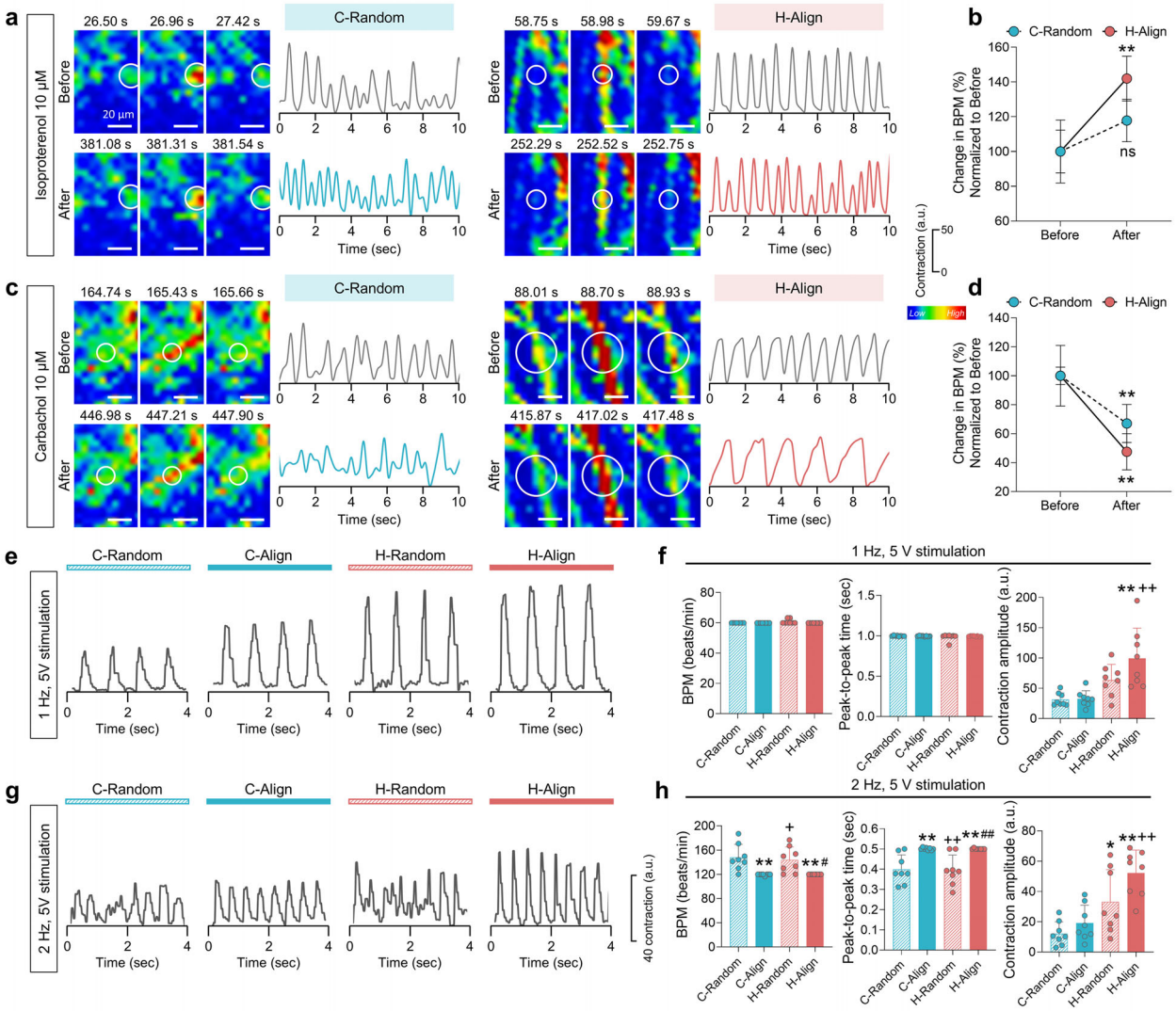

FIGURE 6 | Aligned HEM enhances the contractile function of CiCMs. (a) Representative Ca^{2+} fluorescence time-lapse images and patterns visualized with Fluo-4-AM of CiCMs under C-Random and H-Align conditions before and after 10 μm isoproterenol treatment (scale bars = 20 μm). White dashed circles indicate regions used for fluorescence intensity analysis. (b) Normalized changes in beats per minute (BPM) following 10 μM isoproterenol treatment ($n = 6$; two-way ANOVA followed by Tukey's multiple comparisons test, ns; not significant, $^{**}p < 0.01$ vs. Before group). (c) Representative Ca^{2+} fluorescence images and traces before and after 10 μM carbachol treatment (scale bars = 20 μm). White dashed circles indicate analyzed regions. (d) Normalized BPM changes after 10 μM carbachol treatment ($n = 6$; two-way ANOVA followed by Tukey's multiple comparisons test, $^{**}p < 0.01$ vs. Before group). (e) Contraction curves of CiCMs under electrical stimulation at 1 Hz. (f) Quantification of BPM, peak-to-peak time, and contraction amplitude analyzed using MUSCLEMOTION ($n = 8$; one-way ANOVA followed by Tukey's multiple comparisons test, $^{**}p < 0.01$ vs. C-Random; $^{++}p < 0.01$ vs. C-Align). (g) Contraction curves under electrical stimulation at 2 Hz. (h) Quantitative analysis of BPM, peak-to-peak time, and contraction amplitude based on contraction curves ($n = 8$; one-way ANOVA followed by Tukey's multiple comparisons test, $^{*}p < 0.05$, $^{**}p < 0.01$ vs. C-Random; $^{+}p < 0.05$, $^{++}p < 0.01$ vs. C-Align, $^{\#}p < 0.05$, $^{\#\#}p < 0.01$ vs. H-Random). All data are presented as means ± S.D.

H-Align, showing a 3.04-fold increase over C-Align and a 1.57-fold increase over H-Random (Figure 6e,f; Movie S1). Under high-frequency stimulation at 2 Hz with 5 V, only the aligned groups responded precisely at 120 BPM with a 0.5-s peak-to-peak interval, maintaining synchronous contraction. In contrast, the random groups exhibited irregular or unsynchronized patterns. Although the contraction amplitude decreased in all groups at 2 Hz compared with 1 Hz, the H-Align group maintained the highest amplitude among all conditions (Figure 6g,h; Movie S2). The superior contraction amplitude observed in H-Align is consistent with its more organized myofibrillar structure, polarized Cx43 distribution, and improved calcium-handling capacity. These features indicate that aligned HEM enhances excitation–contraction coupling, supporting more stable and mature electrophysiological behavior in CiCMs [57].

3 | Conclusions

This study provides evidence that alignment and biochemical compositions of cardiac ECM are associated with coordinated nuclear and chromatin remodeling events that accompany CiCM maturation. Using a 3D anisotropic HEM system, we demonstrate that matrix alignment enhances cytoskeletal organization

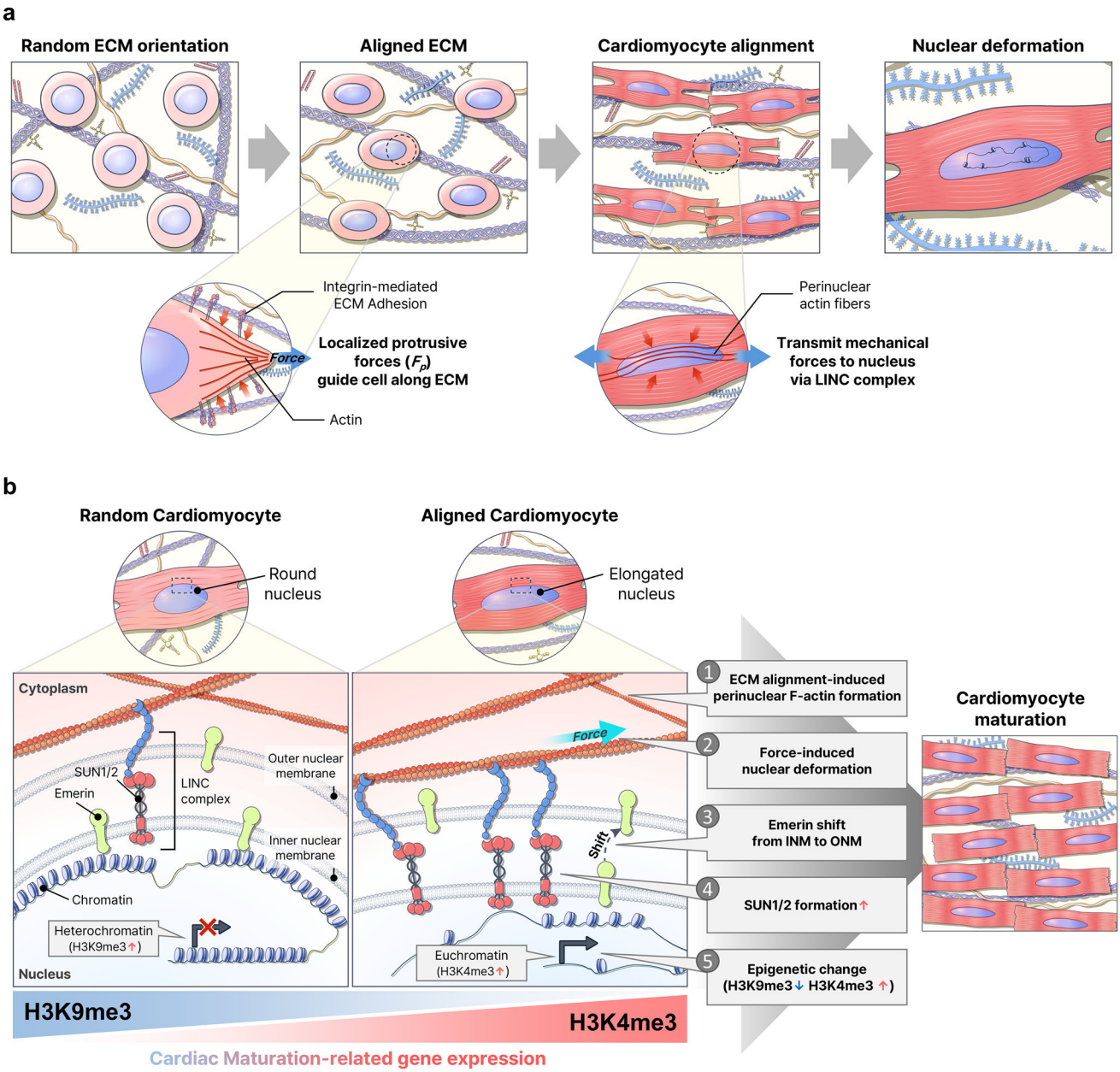

FIGURE 7 | Proposed mechanotransductive model for cardiomyocyte maturation in 3D-aligned HEM. (a) Conceptual model illustrating the progressive alignment and nuclear deformation of cardiomyocytes as they sense and adapt to the anisotropic ECM environment in response to 3D-aligned HEM. (b) Schematic of the mechanotransductive cascade that triggers a series of events, from nuclear morphological changes to epigenetic modifications, in cardiomyocytes aligned by 3D HEM.

and perinuclear actin accumulation, generating directional tension that is associated with nuclear elongation and envelope remodeling (Figure 7a). Functional inhibition experiments further demonstrate that ROCK-dependent cytoskeletal tension is required for alignment-associated nuclear deformation and chromatin remodeling.

This effect was especially pronounced in the HEM condition (Figure 1), likely due to heart-specific ECM-integrin interactions involving ligands such as collagen I/IV, fibronectin, and laminin, which engage integrins like $\alpha1\beta1$, $\alpha5\beta1$, and $\alpha7\beta1$ [6, 58, 59]. As a result, HEM scaffolds facilitate stronger cytoskeletal tension and alignment than single-component collagen matrices [58, 60].

Nuclear deformation under aligned conditions was accompanied by redistribution of emerin to the ONM and increased SUN1/2 expression (Figure 7b). Emerin translocation has been associated with altered heterochromatin organization and histone modification patterns in mechanically stressed cells, suggesting a potential link between nuclear envelope remodeling and chromatin state regulation [33, 34, 61]. Increased SUN1/2 expression under alignment suggests that mechanical cues regulate LINC complex composition. Although the roles of the SUN family in cardiomyocytes remain poorly characterized, emerging evidence indicates that SUN1/2 act as mechanoresponsive regulators in other contexts, such as chromatin reorganization during macrophage polarization, supporting their potential sensitivity to

mechanical and environmental inputs in CiCMs [62]. Together, these findings suggest that anisotropic ECM alignment is coupled to remodeling at the cytoskeletal-nuclear interface. Although transient nuclear localization of YAP/TAZ was observed as an early response to ECM anisotropy, chromatin decondensation and histone modification changes persisted beyond this initial signaling phase. This temporal dissociation suggests that early mechanosensitive signaling events precede and may contribute to longer-lasting chromatin states. In line with prior studies [63–66], these findings support an association between early mechanical inputs and sustained epigenetic reorganization.

Mechanical characterization revealed that matrix alignment did not alter bulk stiffness within the same hydrogel system (Figure S2), indicating that the observed nuclear and epigenetic changes cannot be attributed to stiffness differences alone. At the same time, decellularized ECM systems inherently integrate multiple biochemical parameters, including ligand density, ECM composition, and integrin engagement, which cannot be fully decoupled from structural cues. Therefore, the nuclear and chromatin responses observed here likely reflect the combined influence of anisotropic architecture and cardiac-specific biochemical composition, rather than being attributable to either factor independently. Future studies employing compositionally defined or modular matrices will be required to isolate the relative contributions of each factor.

Functionally, this integrated mechano-nuclear signaling was associated with enhanced structural organization, metabolic maturation, and electrical responsiveness of CiCMs (Figures 5 and 6). However, compared with primary cardiomyocytes and advanced hiPSC-CM maturation systems, certain aspects of structural and electrophysiological maturation remained incomplete, highlighting the need for additional conditioning cues, such as prolonged culture or electrical stimulation, to achieve more fully mature phenotypes.

In conclusion, this work delineates how anisotropic cardiac ECM cues engage cytoskeletal tension, nuclear architecture, and chromatin states in association with the functional maturation of CiCMs. The anisotropic HEM hydrogel provides a tunable, tissue-specific material system that drives structural, transcriptional, and electrophysiological remodeling. More broadly, the mechanistic principles identified here offer an insight applicable to regenerative medicine and tissue engineering, where material-guided control of cell structure and function remains a central challenge.

4 | Experimental Section

4.1 | Primary Mouse Embryonic Fibroblast (PMEF) Culture

All animal procedures were approved by the Institutional Animal Care and Use Committee (IACUC) of the Yonsei University Health System (permit number: IACUC-2023-0055). PMEFs were isolated from embryonic day 13.5 (E13.5) ICR mouse embryos (Orient Bio, Seongnam, Korea) following previously established protocols [6, 67]. Briefly, embryos were dissected and washed in Dulbecco's Phosphate-Buffered Saline (DPBS; Sigma–Aldrich, St. Louis, MO, USA). The heads, limbs, tails, internal organs, and spinal columns were removed, and the remaining tissues were minced into small pieces. The minced tissues werstudy e thoroughly washed with DPBS to eliminate residual blood. For PMEF isolation, the prepared tissue fragments were seeded onto T75 flasks pre-coated with 0.2% (w/v) gelatin (Sigma–Aldrich). The isolated PMEFs were cultured in Dulbecco's Modified Eagle Medium (DMEM; Thermo Fisher Scientific, Waltham, MA, USA) supplemented with 10% (v/v) fetal bovine serum (FBS; Thermo Fisher Scientific), 1% (v/v) penicillin-streptomycin (Thermo Fisher Scientific), and 1% (v/v) non-essential amino acids (NEAA; Thermo Fisher Scientific). Cells were maintained at 37 °C in a 5% CO_2 humidified incubator, with media replacement on the following day. The PMEFs were utilized for CiCM reprogramming on day 2 after tissue seeding.

4.2 | Induction of PMEFs into CiCMs

Six-well plates were coated with Matrigel Matrix (Corning Incorporated, Corning, NY, USA) diluted 1:50 (v/v) in DMEM/F12 (Thermo Fisher Scientific) and incubated at 37 °C for 1–2 h prior to cell seeding. PMEFs were dissociated using 0.05% (w/v) Trypsin-EDTA (Thermo Fisher Scientific) and filtered through a 100-µm cell strainer to obtain a single-cell suspension. Cells were seeded onto the coated plates at a density of 2.5×10^4 cells mL^{-1}. After 4 h of attachment, the medium was replaced with CiCM reprogramming medium. The CiCM medium consisted of DMEM/F12 supplemented with 15% (v/v) FBS, 5% (v/v) KnockOut Serum Replacement (Thermo Fisher Scientific), 1% (v/v) penicillin-streptomycin, 1% (v/v) NEAA, 1% (v/v) GlutaMAX (Thermo Fisher Scientific), 0.1 mM β-mercaptoethanol (Thermo Fisher Scientific), and the following small molecules: 10 µm CHIR99021 (#HY-10182, MedChem Express, Monmouth Junction, NJ, USA), 15 µm forskolin (#F-9929, LC Laboratories, Woburn, MA, USA), 2 µm A83-01 (#HY-10432, MedChem Express), and 1 µm SC-1 (#10009557, Cayman Chemical, Ann Arbor, MI, USA) [6, 67]. Cells were cultured at 37 °C in a humidified atmosphere containing 5% CO_2, and the medium was refreshed every other day.

4.3 | Fabrication and Surface Modification of Patterned PDMS Chips

Polydimethylsiloxane (PDMS) chips (1.5 mm in thickness) were fabricated using a duralumin master mold containing a rectangular groove pattern with dimensions of 5 mm (width) × 10 mm (length) × 0.35 mm (depth). Prior to use, the duralumin master was silanized with fluorinated silane (trichloro(1H,1H,2H,2H-perfluorooctyl) silane; Sigma–Aldrich) to facilitate demolding. A PDMS mixture was prepared by combining base and curing agent (Sylgard 184, Dow Corning, Midland, MI, USA) at a 10:1 weight ratio. The mixture was degassed under vacuum and poured onto the silanized mold, followed by a second vacuum degassing step to remove residual air bubbles. The PDMS was cured at 70 °C for 35 min and then gently peeled off from the master to obtain the patterned PDMS replicas.

The PDMS chips were cleaned to remove dust and subsequently sterilized using an autoclave prior to use. To enhance ECM

hydrogel adhesion, the inner surface of the PDMS channels was coated with polydopamine by applying a solution of 2 mg mL^{-1} dopamine hydrochloride (Sigma–Aldrich) dissolved in 10 mM Tris-HCl buffer (pH 8.5). After incubating at room temperature for 3 h, the channels were thoroughly washed with deionized water and air-dried before hydrogel loading.

4.4 | Preparation of COL and HEM Hydrogel

Commercially available type I collagen (COL; #354249, Corning) was supplied in solution form, while heart extracellular matrix (HEM; Regenix™ Heart ECM Powder, Cellartgen, Seoul, Korea) was provided as a lyophilized powder. To prepare the HEM solution, the powder was dissolved at a concentration of 10 in 8 mg mL^{-1} pepsin (Sigma–Aldrich) in 0.02 M hydrochloric acid (Thermo Fisher Scientific) and stirred at 250 rpm at room temperature for 48 h, following the manufacturer's protocol. To prepare the pre-gel solutions of COL and HEM at a final concentration of 5 mg mL^{-1}, the solubilized matrices were diluted with 10× PBS and deionized water. The pH of these solutions was then adjusted to 7.0–7.4 using 0.5 N NaOH. To prepare cell-seeded pre-gel solutions, cells were suspended at a density of 2×10^7 cells mL^{-1}. Both cell-seeded and cell-free pre-gel were then immediately processed using the 3D alignment system for gelation and subsequent experiments.

4.5 | Fibrillar Protein Labeling

For visualization of fibrillar proteins in hydrogels, COL and HEM solutions were labeled with 5-(and-6)-Carboxytetramethylrhodamine succinimidyl ester (5(6)-TAMRA-SE; Thermo Fisher Scientific). 5(6)-TAMRA-SE is an N-hydroxysuccinimide (NHS) ester, which reacts with primary amines on hydrogel proteins to form stable amide bonds, thereby fluorescently labeling collagenous fibrils. COL and HEM solutions were supplemented with 5 μm 5(6)-TAMRA-SE, 10× PBS, and deionized water, and then incubated on ice for 3 h. Following incubation, the mixtures were neutralized with 0.5 N NaOH (Sigma–Aldrich) to achieve a final concentration of 5 mg mL^{-1}. The labeled pre-gel solutions were then gelled at 37 °C for 30 min, washed three times with PBS, and imaged using a confocal microscope (LSM 980, Carl Zeiss, Jena, Germany).

4.6 | Fibril Alignment of COL and HEM Hydrogel

Based on previously described methods, polydopamine-coated PDMS chips were uniaxially pre-stretched along the x-axis from their original length (L) to a stretched state (L + ΔL), corresponding to a strain of ΔL/L = 0.5, to induce alignment of COL and HEM fibrils [14]. The deformation was performed using a customized stretching device. To minimize undesired gelation, neutralized COL and HEM pre-gel solutions were kept on ice. Following this, pre-gel solutions of COL or HEM, with or without cells, were loaded into the pre-stretched PDMS wells. A coverslip was then placed over the loaded channels to provide mechanical confinement. This facilitated the formation of a uniform interface essential for fibril alignment. Partial fibrillogenesis was induced at 37 °C for optimal durations specific to each matrix (4.5 min for COL and 8 min for HEM). Subsequently, mechanical strain was released by returning the PDMS chips from L + ΔL to L, thereby promoting alignment of the forming collagen microfibrils perpendicular to the stretch axis. The PDMS chips were then transferred to 12-well plates and incubated at 37 °C with 5% CO_2 for an additional 30 min to complete the gelation process.

4.7 | Cell Viability Assessment

To evaluate cell viability under alignment-induced stress, a Live/Dead assay was performed on Day 1 using the Live/Dead™ Viability/Cytotoxicity Kit (#L3224, Thermo Fisher Scientific). Cell-seeded hydrogel samples were first washed once with DPBS. A staining solution containing 2 μm calcein-AM and 4 μm ethidium homodimer-1, prepared in DPBS, was applied to the samples. The samples were then incubated at 37 °C with 5% CO_2 for 30 min. After incubation, samples were gently washed once with DPBS. Live cells were stained with calcein-AM (green), while dead cells were labeled with ethidium homodimer-1 (red). Fluorescent images were acquired within 20 min using a fluorescence microscope (EVOS™ M5000, Thermo Fisher Scientific).

4.8 | Turbidity Assay for Fibrillogenesis Kinetics

To analyze the fibrillogenesis kinetics of COL and HEM, turbidity measurements were performed. Pre-gel solutions of 5 mg mL^{-1} COL and HEM were loaded into a clear, flat-bottom 96-well plate at 200 μL per well. To prevent premature gelation, the samples were kept on ice prior to measurement. Absorbance at 450 nm was recorded at 1-min intervals for 90 min at 37 °C using a FlexStation 3 Multi-Mode Microplate Reader (Molecular Devices, San Jose, CA, USA). The measured absorbance data were normalized to PBS control, and the normalized absorbance (NA) was calculated using the following equation:

$$NA = \frac{A - A_0}{A_{max} - A_0}$$

where A is the absorbance at a given time point, A_0 is the initial absorbance, and A_{max} is the maximum absorbance recorded during the measurement. The lag phase (t_{lag}) was determined as the x-intercept of the tangent line at the point of maximum slope of the curve. The time to half gelation ($t_{1/2}$), indicative of the time for 50% gel formation, was defined as the time when the normalized absorbance reached 0.5. The gelation rate (S) was calculated as the maximum slope of the absorbance curve.

4.9 | Measurement of Rheological Properties of Hydrogels

To characterize the mechanical properties of the hydrogel scaffolds, the rheological profiles of cell-free COL, HEM hydrogels were evaluated using a rotating rheometer (MCR102; Anton Paar, Ashland, VA, USA) equipped with an 8 mm-diameter parallel-plate probe. A frequency sweep was performed from 0.1 to 1 Hz at a constant strain of 1%. The storage modulus and loss modulus were recorded throughout the frequency range. For comparison

among groups, the elastic modulus was determined by calculating the average storage modulus at 1 Hz.

4.10 | Immunofluorescence Staining

CiCMs encapsulated in 3D hydrogels were washed twice with PBS and fixed with 4% paraformaldehyde (Sigma–Aldrich) at room temperature for 30 min. Following fixation, the samples were transferred to 2 mL microtubes and permeabilized with 0.2% (v/v) Triton X-100 in PBS for 30 min at room temperature. To distinguish between inner and outer nuclear envelope localization of emerin, alternative permeabilization protocols were employed: 0.3% Triton X-100 in PBS for inner membrane staining and 0.003% digitonin in PBS for outer membrane staining, each applied for 30 min at room temperature. Permeabilized samples were then blocked with 5% (w/v) bovine serum albumin (BSA; Fraction V, MP Biomedicals, Irvine, CA, USA) in PBS for 2 h at room temperature. After blocking, the samples were incubated with primary antibodies at 4 °C for 24 h. The following primary antibodies were used: anti-rabbit emerin (1:350; #30853, Cell Signaling Technology, Danvers, MA, USA), anti-mouse Lamin A/C (1:200; #4777, Cell Signaling Technology), anti-mouse Yes-associated protein (YAP; 1:70; #sc-101199, Santa Cruz Biotechnology), anti-rabbit H3K9me3 (1:500; #ab8898, Abcam, Cambridge, UK), and anti-rabbit H3K4me3 (1:500; #ab8580, Abcam), anti–mouse α-actinin (1:500; #A7811, Sigma–Aldrich), anti-mouse cTnT (1:200; #MA5-12960, Thermo Fisher Scientific), anti-rabbit Cx43 (1:300; #C6219, Sigma–Aldrich). Following primary antibody incubation, the samples were washed at least three times with PBS at 1-h intervals. Samples were then incubated with the appropriate secondary antibodies at 4 °C for 24 h. The following secondary antibodies were used: anti-mouse Alexa Fluor 488 (1:200; #A11001, Thermo Fisher Scientific), anti-mouse Alexa Fluor 594 (1:200; #A11005, Thermo Fisher Scientific), and anti-rabbit Alexa Fluor 594 (1:200; #A11012, Thermo Fisher Scientific). For cytoskeletal visualization, Phalloidin-iFluor 594 Reagent (1:1000; #ab176757, Abcam) and Phalloidin-iFluor 488 Reagent (1:1000; #ab176753, Abcam) were used to stain filamentous actin (F-actin). T-tubule structures were visualized using FITC-conjugated wheat germ agglutinin (WGA; 5 μg mL^{-1}; #L4895, Sigma–Aldrich). Nuclei were counterstained with 4′,6-diamidino-2-phenylindole dihydrochloride (DAPI; TCI Chemicals, Tokyo, Japan). All images were acquired using a confocal laser scanning microscope (LSM 980, Carl Zeiss).

4.11 | Image Analysis

Image analysis was performed using ImageJ (National Institutes of Health, Bethesda, MD, USA), ZEN software (Carl Zeiss), or MATLAB (MathWorks, Natick, MA, USA). Morphological and molecular characteristics of each experimental group were quantified based on fluorescence images.

The orientation of fibrils, cells, and nuclei was analyzed using the OrientationJ plugin in ImageJ, as previously reported [14]. For the OrientationJ distribution analysis, the local window δ of the structure tensor was set to 5 pixels. The polar frequency data obtained from the plugin were normalized. Nuclear morphology, including circularity and nuclear area, was quantified from DAPI-stained images by defining individual nuclear regions of interest (ROIs) and measuring each parameter using ImageJ.

Chromatin condensation parameters (CCP) were analyzed as previously described using MATLAB [41]. Briefly, nuclear regions were segmented from DAPI images, edges were detected using Sobel filters, and condensation parameters were extracted from the processed images.

For fluorescence intensity analysis of F-actin, emerin, YAP, H3K9me3, and H3K4me3, all images were acquired using identical laser power and detector gain settings on a confocal laser scanning microscope to ensure comparable fluorescence signal levels across groups. Acquired images were converted to 8-bit grayscale using ImageJ. ROIs were defined in the perinuclear or nuclear regions based on the DAPI channel, and the mean gray value was measured for each ROI.

Sarcomere length was quantified from α-actinin–stained images using ZEN software. The sarcomere length was calculated by measuring the distance between adjacent peaks in the intensity profile plot. The area positive for cardiac markers was quantified using ImageJ.

4.12 | Western Blotting

Samples were homogenized in radioimmunoprecipitation assay (RIPA) buffer (#R0278, Sigma–Aldrich) supplemented with a protease inhibitor cocktail (#11836170001, Roche, Mannheim, Germany) for 30 min on ice. The protein-containing supernatant was obtained by centrifugation at 13 000 rpm for 20 min at 4 °C. Protein concentration was determined using a BCA protein assay kit (#T9300A, Takara Bio Inc., Kusatsu, Shiga, Japan). For western blot analysis, 20 μg of total protein was resolved on 10% SDS-PAGE gel and transferred onto nitrocellulose membranes (Cytiva, Marlborough, MA, USA). Membranes were blocked with 5% (w/v) skim milk in tris-buffered saline with 0.1% Tween-20 (TBST) for 1 h at room temperature, followed by incubation with primary antibodies overnight at 4 °C on a shaker. The following primary antibodies were used: anti-rabbit SUN1 (1:2000; #GTX637784, GeneTex, Irvine, CA, USA), anti-rabbit SUN2 (1:1500; #ab124916, Abcam, Cambridge, UK), and anti-rabbit GAPDH (1:20,000; #BS-2188R, Bioss, Woburn, MA, USA). After thorough washing with TBST, membranes were incubated with HRP-conjugated goat anti-rabbit IgG secondary antibody (#31460, Thermo Fisher Scientific) for 1 h at room temperature. Protein bands were detected using an ECL detection kit (Abbkine, Wuhan, Hubei, China) and visualized with an X-ray film processor (#CP1000, AGFA, Mortsel, Belgium). Densitometry analysis of the protein bands was performed using ImageJ software.

4.13 | ROCK Inhibition and siRNA-Mediated Knockdown

To functionally disrupt cytoskeletal tension, CiCMs were treated with Y-27632 dihydrochloride (HY-10583, MedChem Express), a inhibitor of Rho kinase (ROCK). Prior to encapsulation into 3D HEM hydrogels, cells were pre-incubated with 10 μm Y-27632 for 2 h to ensure early inhibition of actomyosin contractility.

Following 3D encapsulation and alignment, hydrogel constructs were cultured in complete medium supplemented with 50 μm Y-27632 for an additional 48 h.

For small interfering RNA (siRNA)-mediated silencing of the *Sun1* and *Sun2*, CiCMs were transfected with siRNAs targeting mouse *Sun1* (ID: 77053) and *Sun2* (ID: 223697) using Lipofectamine™ RNAiMAX Transfection Reagent (Thermo Fisher Scientific), according to the manufacturer's instructions. Predesigned AccuTarget™ Genome-wide siRNAs (Bioneer, Daejeon, Korea) were used. A non-targeting AccuTarget™ Negative Control siRNA served as the control. Transfections were performed under 2D culture conditions for 24 h prior to 3D encapsulation. Following encapsulation, cells were maintained within 3D HEM hydrogels for an additional 48 h to allow sustained gene knockdown. All siRNAs were diluted in Opti-MEM™ Reduced Serum Medium (Thermo Fisher Scientific), and antibiotic-free complete culture medium was used throughout the transfection process. For single-gene knockdown, siSun1 or siSun2 was used at a final concentration of 50 nM. For double knockdown, siSun1 and siSun2 were combined at equal concentrations (25 nM each), yielding a total siRNA concentration of 50 nM. Control siRNA was also used at 50 nM.

4.14 | Isolation and Culture of Neonatal Mouse Cardiomyocytes (nCMs)

All animal procedures were approved by the Institutional Animal Care and Use Committee (IACUC) of the Yonsei University Health System (permit number: IACUC-2022-0157). nCMs were isolated from 1- to 3-day-old postnatal ICR mice according to a previously established protocol with minor modifications [68]. To preserve myocardial viability during isolation, excised hearts were immediately transferred to ice-cold DPBS supplemented with 20 mM 2,3-butanedione monoxime (BDM; Sigma–Aldrich). The ventricles were minced into fragments in isolation media consisting of HBSS supplemented with 0.2 mM BDM and 0.0125% (w/v) Trypsin-EDTA, followed by overnight enzymatic digestion at 4 °C with gentle agitation. On the following day, the supernatant was removed, and the tissue fragments were resuspended in a 1:1 mixture of digestion media and L-15/BDM solution. The digestion media was composed of L-15 medium (Thermo Fisher Scientific) containing 20 mM BDM and 1.5 mg mL^{-1} collagenase/dispase (Roche). The suspension was oxygenated for 1 min and incubated at 37 °C for 30 min with agitation. The digested tissue was mechanically dissociated and passed through a 100-μm cell strainer. The collected cell suspension was centrifuged at 100×g for 5 min, and the pellet was resuspended in plating medium. The plating medium consisted of DMEM supplemented with 1% (v/v) penicillin-streptomycin, 19% (v/v) Medium 199 (Thermo Fisher Scientific), 10% (v/v) horse serum (Thermo Fisher Scientific), and 5% (v/v) FBS. The nCMs were then seeded onto 12-well plates pre-coated with 0.05 mg mL^{-1} Type I collagen at a density of 7×10^5 cells mL^{-1}. After 24 h, the plating media was replaced with maintenance media, which consisted of DMEM supplemented with 1% (v/v) penicillin-streptomycin, 17% (v/v) Medium 199, and 4% (v/v) horse serum. The nCMs were maintained at 37 °C in a humidified atmosphere with 5% CO_2 for 4 days prior to being harvested for further analysis.

4.15 | Quantitative Real-Time Polymerase Chain Reaction (qPCR)

Total RNA was extracted using a MiniBEST Universal RNA extraction kit (Takara) following the manufacturer's instructions. RNA purity and concentration were assessed by spectrophotometry (NanoDrop 1000, Thermo Fisher Scientific). Complementary DNA was subsequently synthesized from the total RNA using a PrimeScript II First-Strand cDNA synthesis kit (Takara). qPCR amplification was performed using the TaqMan Fast Universal PCR Master Mix (Thermo Fisher Scientific) on a QuantStudio 3 Real-Time PCR System (Applied Biosystems, Waltham, MA, USA). The following TaqMan Gene Expression Assays (Thermo Fisher Scientific) were employed: *Nkx2-5* (Mm01309813_s1), *Mef2c* (Mm01340842_m1), *Myh7* (Mm00600555_m1), *Cpt1b* (Mm00487191_g1), *Tfam* (Mm00447485_m1), *Ppara* (Mm00440939_m1), *Nfe2l2* (Mm00477784_m1), *Scn5a* (Mm01342518_m1), and *Gja1*(Mm01179639_s1). Relative gene expression was calculated using the comparative cycle threshold (Ct) method and normalized to that of the endogenous control gene, *Gapdh* (Mm99999915_g1).

To validate siRNA-mediated knockdown efficiency of *Sun1* and *Sun2*, SYBR Green-based qPCR was additionally performed. Reactions were conducted on a QuantStudio 3 system using PowerUp™ SYBR™ Green Master Mix (Thermo Fisher Scientific) and gene-specific primers synthesized by Macrogen (Seoul, Korea). Primer sequences were as follows: *Sun1* (F: ATCCGAGGCTATTGTGTCTGCC; R: CTCCAGAGCAAAGTCCACCATC), *Sun2* (F: TGACTCTGAAGCAGAACTCGGTG; R: CCTGTCTCCAAGAAGGAACTGC), and *Gapdh* (F: CATCACTGCCACCCAGAAGACTG; R: ATGCCAGTGAGCTTCCCGTTCAG). For SYBR Green–based assays, gene expression levels were normalized to the reference gene *Gapdh*, and relative expression was calculated using the comparative Ct method.

4.16 | Calcium Imaging

For calcium imaging, cells were loaded with the calcium indicator Fluo-4 AM (Thermo Fisher Scientific) at a concentration of 3 μm for 30min at 37 °C. Subsequently, cells were washed with basal medium (DMEM/F12) excluding small molecules. To test the effects of drugs, CiCMs were treated with either isoproterenol (Sigma–Aldrich) or carbachol (Sigma–Aldrich) at a concentration of 10 μm. Changes in calcium transients were observed in the CiCMs after the addition of each drug. Serial images of calcium transients were acquired using a confocal microscope (LSM 710, Carl Zeiss). ROIs were selected for analysis, and changes in fluorescence intensity were quantified using ZEN software. Normalized peak amplitude and frequency of calcium transients were then manually calculated from the time-lapse images.

4.17 | Assessment of Contractile Function Under Electrical Stimulation

Cardiomyocyte Contractility was assessed using video recordings analyzed with the MUSCLEMOTION plugin for ImageJ [69,

70]. Videos were captured using a CKX53 microscope (Olympus, Tokyo, Japan) under spontaneous or electrically stimulated conditions and saved in MP4 format. Prior to analysis, video files were converted into sequential TIFF image frames using FFmpeg. The extracted frames were imported into MUSCLEMOTION to quantify contraction dynamics. Parameters including BPM, peak-to-peak time, and contraction amplitude were calculated as the average of multiple contraction peaks within each ROI. Electrical stimulation was delivered using a WPG100e electrochemical workstation (WonATech, Seoul, Korea) with biphasic pulses under the following conditions: 5 V, 100 ms pulse width, 1 Hz frequency, and 5 V, 2 ms pulse width, 2 Hz frequency.

4.18 | Statistical Analysis

All data are presented as the mean ± standard deviation (SD). The sample size (n) indicated in the figure legends represents the number of biological replicates. Statistical analyses were performed using GraphPad Prism 8 (GraphPad Software, La Jolla, CA, USA). Unpaired two-tailed Student's t-tests were used for comparisons between two groups. One-way analysis of variance (ANOVA) with Tukey's post-hoc test was applied for multiple group comparisons, and two-way ANOVA followed by Tukey's multiple comparisons test was used when two independent variables were involved. For correlation analyses, two-tailed Pearson's correlation coefficient (R) was calculated to assess linear relationships between variables. p-values less than 0.05 were considered statistically significant.

Author Contributions

Y.J., S.-W.C., and N.C. conceived the study and supervised the project. S.J.S. designed and conducted the experiments and performed data analysis. M.J.L. provided guidance on the use of the hydrogel system and performed hydrogel characterization. H.W.K. developed the devices and PDMS molds required for ECM alignment. S.B. and S.-K.C. provided technical support for the functional inhibition assays. S.J.S., and Y.J. wrote the manuscript with input from all authors. All authors reviewed and approved the manuscript.

Acknowledgements

This work was supported by the National Research Foundation of Korea (NRF) grant funded by the Korea government (MSIT) (RS-2021-NR061930), the Nano & Material Technology Development Program through the NRF funded by MSIT (RS-2025-25424498), and Institute of Basic Science (IBS) (IBS-R026-D1). This work was also supported by the Technology Innovation Program (20024298, Development of highly functional decellularized matrices for the production and implantation of organ-like constructs) funded by the Ministry of Trade, Industry and Resources (MOTIR, Korea). The authors also acknowledge MID (Medical Illustration & Design), a member of the Medical Research Support Services of Yonsei University College of Medicine, for their support with schematic illustrations.

Funding

This work was supported by the Ministry of Science and ICT through National Research Foundation of Korea (NRF): RS-2021-NR061930, RS-2025-25424498, Ministry of Trade, Industry and Energy through Korea Planning & Evaluation Institute of Industrial Technology (KEIT): 20024298, Institute for Basic Science: IBS-R026-D1.

Conflicts of Interest

The authors declare no conflicts of interest.

Data Availability Statement

The data that support the findings of this study are available from the corresponding author upon reasonable request.

References

1. Y. Guo and W. T. Pu, "Cardiomyocyte Maturation: New Phase in Development," *Circulation Research* 126, no. 8 (2020): 1086–1106.

2. E. Karbassi, A. Fenix, S. Marchiano, et al., "Cardiomyocyte Maturation: Advances in Knowledge and Implications for Regenerative Medicine," *Nature Reviews Cardiology* 17, no. 6 (2020): 341–359.

3. W. Bian, C. P. Jackman, and N. Bursac, "Controlling the Structural and Functional Anisotropy of Engineered Cardiac Tissues," *Biofabrication* 6, no. 2 (2014): 024109.

4. J. Veldhuizen, R. Q. Migrino, and M. Nikkhah, "Three-Dimensional Microengineered Models of Human Cardiac Diseases," *Journal of Biological Engineering* 13 (2019): 29.

5. Y. Fu, C. Huang, X. Xu, et al., "Direct Reprogramming of Mouse Fibroblasts Into Cardiomyocytes With Chemical Cocktails," *Cell Research* 25, no. 9 (2015): 1013–1024.

6. Y. Jin, H. Kim, S. Min, et al., "Three-Dimensional Heart Extracellular Matrix Enhances Chemically Induced Direct Cardiac Reprogramming," *Science Advances* 8, no. 50 (2022): abn5768.

7. G. E. Brown, Y. D. Han, A. R. Michell, et al., "Engineered Cocultures of Ipsc-Derived Atrial Cardiomyocytes and Atrial Fibroblasts for Modeling Atrial Fibrillation," *Science Advances* 10, no. 3 (2024): adg1222.

8. M. Tiburcy, J. E. Hudson, P. Balfanz, et al., "Defined Engineered Human Myocardium With Advanced Maturation for Applications in Heart Failure Modeling and Repair," *Circulation* 135, no. 19 (2017): 1832–1847.

9. I. U. Kim, J. Kim, and J. S. Jeon, "Development of a 3D Vascularized Skeletal Muscle Model Using Bi-Layered Seeding Methods," *BioChip Journal* 19, no. 4 (2025): 807–817.

10. S. Dong, K. Guo, N. Zhao, and Y. Xu, "Au@pt Nanoparticles Enhance Maturation and Contraction of Mouse Embryonic Stem Cells-Derived and Neonatal Mouse Cardiomyocytes," *Tissue Engineering and Regenerative Medicine* 22, no. 5 (2025): 611–625.

11. S. Min, S. Kim, W.-S. Sim, et al., "Versatile Human Cardiac Tissues Engineered With Perfusable Heart Extracellular Microenvironment for Biomedical Applications," *Nature Communications* 15, no. 1 (2024): 2564.

12. M. Mao, J. He, Z. Li, K. Han, and D. Li, "Multi-Directional Cellular Alignment in 3D Guided by Electrohydrodynamically-Printed Microlattices," *Acta Biomaterialia* 101 (2020): 141–151.

13. S. Choi, K. Y. Lee, S. L. Kim, et al., "Fibre-Infused Gel Scaffolds Guide Cardiomyocyte Alignment in 3D-Printed Ventricles," *Nature Materials* 22, no. 8 (2023): 1039–1046.

14. Y. Jin, E. J. Jeon, S. Jeong, et al., "Reconstruction of Muscle Fascicle-Like Tissues by Anisotropic 3D Patterning," *Advanced Functional Materials* 31, no. 25 (2021): 2006227.

15. S. Chen, C. Xie, X. Long, et al., "Development of Electrospinning Setup for Vascular Tissue-Engineering Application With Thick-Hierarchical Fiber Alignment," *Tissue Engineering and Regenerative Medicine* 22, no. 2 (2025): 195–210.

16. A. C. B. Allen, E. Barone, N. Momtahan, et al., "Temporal Impact of Substrate Anisotropy on Differentiating Cardiomyocyte Alignment and Functionality," *Tissue Engineering Part A* 25, no. 19-20 (2019): 1426–1437.

17. A. J. Maniotis, C. S. Chen, and D. E. Ingber, "Demonstration of Mechanical Connections Between Integrins, Cytoskeletal Filaments,

and Nucleoplasm That Stabilize Nuclear Structure," *Proceedings of the National Academy of Sciences* 94, no. 3 (1997): 849–854.

18. T. Bouzid, E. Kim, B. D. Riehl, et al., "The Linc Complex, Mechanotransduction, and Mesenchymal Stem Cell Function and Fate," *Journal of Biological Engineering* 13 (2019): 68.

19. Y. Song, J. Soto, S. Y. Wong, et al., "Biphasic Regulation of Epigenetic State by Matrix Stiffness During Cell Reprogramming," *Science Advances* 10, no. 7 (2024): adk0639.

20. M. Song, Y. Jang, S. J. Kim, and Y. Park, "Cyclic Stretching Induces Maturation of Human-Induced Pluripotent Stem Cell-Derived Cardiomyocytes Through Nuclear-Mechanotransduction," *Tissue Engineering and Regenerative Medicine* 19, no. 4 (2022): 781–792.

21. Z. Yu, K. Wu, C. Fan, et al., "Viscoelastic Hydrogel Promotes Disc Mechanical Homeostasis Repair and Delays Intervertebral Disc Degeneration via the Yes-Associated Protein Pathway," *Biomaterials Research* 29 (2025): 0150.

22. S. G. Alam, Q. Zhang, N. Prasad, et al., "The Mammalian Linc Complex Regulates Genome Transcriptional Responses to Substrate Rigidity," *Scientific Reports* 6 (2016): 38063.

23. S.-M. Park, J.-H. Lee, K. S. Ahn, et al., "Cyclic Stretch Promotes Cellular Reprogramming Process Through Cytoskeletal-Nuclear Mechano-Coupling and Epigenetic Modification," *Advanced Science* 10, no. 32 (2023): 2303395.

24. C.-C. Hsu, A. Serio, S. Gopal, et al., "Biophysical Regulations of Epigenetic State and Notch Signaling in Neural Development Using Microgroove Substrates," *ACS Applied Materials & Interfaces* 14, no. 29 (2022): 32773–32787.

25. S. H. Kim, S.-K. Im, S.-J. Oh, et al., "Anisotropically Organized Three-Dimensional Culture Platform for Reconstruction of a Hippocampal Neural Network," *Nature Communications* 8, no. 1 (2017): 14346.

26. G. Thrivikraman, A. Jagiello, V. K. Lai, et al., "Cell Contact Guidance via Sensing Anisotropy of Network Mechanical Resistance," *Proceedings of the National Academy of Sciences* 118, no. 29 (2021): 2024942118.

27. C. Leclech and C. Villard, "Cellular and Subcellular Contact Guidance on Microfabricated Substrates," *Frontiers in Bioengineering and Biotechnology* 8 (2020): 551505.

28. S. B. Khatau, C. M. Hale, P. J. Stewart-Hutchinson, et al., "A Perinuclear Actin Cap Regulates Nuclear Shape," *Proceedings of the National Academy of Sciences* 106, no. 45 (2009): 19017–19022.

29. A. B. Chambliss, S. B. Khatau, N. Erdenberger, et al., "The Linc-Anchored Actin Cap Connects the Extracellular Milieu to the Nucleus for Ultrafast Mechanotransduction," *Scientific Reports* 3, no. 1 (2013): 1087.

30. L. M. Hoffman, M. A. Smith, C. C. Jensen, et al., "Mechanical Stress Triggers Nuclear Remodeling and the Formation of Transmembrane Actin Nuclear Lines With Associated Nuclear Pore Complexes," *Molecular Biology of the Cell* 31, no. 16 (2020): 1774–1787.

31. B. Seelbinder, S. Ghosh, S. E. Schneider, et al., "Nuclear Deformation Guides Chromatin Reorganization in Cardiac Development and Disease," *Nature Biomedical Engineering* 5, no. 12 (2021): 1500–1516.

32. Y. Kalukula, A. D. Stephens, J. Lammerding, and S. Gabriele, "Mechanics and Functional Consequences of Nuclear Deformations," *Nature Reviews Molecular Cell Biology* 23, no. 9 (2022): 583–602.

33. N. Marano and J. M. Holaska, "The Role of Inner Nuclear Membrane Protein Emerin in Myogenesis," *The FASEB Journal* 39, no. 7 (2025): 70514.

34. H. Q. Le, S. Ghatak, C.-Y. C. Yeung, et al., "Mechanical Regulation of Transcription Controls Polycomb-Mediated Gene Silencing During Lineage Commitment," *Nature Cell Biology* 18, no. 8 (2016): 864–875.

35. M. L. Lombardi, D. E. Jaalouk, C. M. Shanahan, B. Burke, K. J. Roux, and J. Lammerding, "The Interaction Between Nesprins and Sun Proteins at the Nuclear Envelope is Critical for Force Transmission Between the Nucleus and Cytoskeleton," *Journal of Biological Chemistry* 286, no. 30 (2011): 26743–26753.

36. W. Xie, X. Wei, H. Kang, et al., "Static and Dynamic: Evolving Biomaterial Mechanical Properties to Control Cellular Mechanotransduction," *Advanced Science* 10, no. 9 (2023): 2204594.

37. A. Tajik, Y. Zhang, F. Wei, et al., "Transcription Upregulation via Force-Induced Direct Stretching of Chromatin," *Nature Materials* 15, no. 12 (2016): 1287–1296.

38. S. Dupont, L. Morsut, M. Aragona, et al., "Role of Yap/Taz in Mechanotransduction," *Nature* 474, no. 7350 (2011): 179–183.

39. A. Elosegui-Artola, I. Andreu, A. E. M. Beedle, et al., "Force Triggers Yap Nuclear Entry by Regulating Transport Across Nuclear Pores," *Cell* 171, no. 6 (2017): 1397–1410.e14.

40. C. J. Boogerd, I. Perini, E. Kyriakopoulou, et al., "Cardiomyocyte Proliferation is Suppressed by Arid1a-Mediated Yap Inhibition During Cardiac Maturation," *Nature Communications* 14, no. 1 (2023): 4716.

41. J. Irianto, D. A. Lee, and M. M. Knight, "Quantification of Chromatin Condensation Level by Image Processing," *Medical Engineering & Physics* 36, no. 3 (2014): 412–417.

42. A. Soufi, M. F. Garcia, A. Jaroszewicz, N. Osman, M. Pellegrini, and K. S. Zaret, "Pioneer Transcription Factors Target Partial DNA Motifs on Nucleosomes to Initiate Reprogramming," *Cell* 161, no. 3 (2015): 555–568.

43. H. Wang, Y. Yang, J. Liu, and L. Qian, "Direct Cell Reprogramming: Approaches, Mechanisms and Progress," *Nature Reviews Molecular Cell Biology* 22, no. 6 (2021): 410–424.

44. A. J. Bannister and T. Kouzarides, "Regulation of Chromatin by Histone Modifications," *Cell Research* 21, no. 3 (2011): 381–395.

45. C. Cao, L. Li, Q. Zhang, et al., "Nkx2.5: A Crucial Regulator of Cardiac Development, Regeneration and Diseases," *Frontiers in Cardiovascular Medicine* 10 (2023): 1270951.

46. S. Takashima, S. Usui, O. Inoue, et al., "Myocyte-Specific Enhancer Factor 2c Triggers Transdifferentiation of Adipose Tissue-Derived Stromal Cells Into Spontaneously Beating Cardiomyocyte-Like Cells," *Scientific Reports* 11, no. 1 (2021): 1520.

47. M. Deogharia and P. Gurha, "Fueling Cardiac Myocyte Proliferation," *The Journal of Cardiovascular Aging* 4, no. 1 (2024): 2.

48. S. A. Murphy, M. Miyamoto, A. Kervadec, et al., "PGC1/PPAR Drive Cardiomyocyte Maturation at Single Cell Level via YAP1 and SF3B2," *Nature Communications* 12, no. 1 (2021): 1648.

49. D. Zhang, Y. Li, D. Heims-Waldron, et al., "Mitochondrial Cardiomyopathy Caused by Elevated Reactive Oxygen Species and Impaired Cardiomyocyte Proliferation," *Circulation Research* 122, no. 1 (2018): 74–87.

50. X. Zhang, L. Ye, H. Xu, et al., "NRF2 is Required for Structural and Metabolic Maturation of Human Induced Pluripotent Stem Cell-Derived Ardiomyocytes," *Stem Cell Research & Therapy* 12, no. 1 (2021): 208.

51. M. J. van Kempen, C. Fromaget, D. Gros, A. F. Moorman, and W. H. Lamers, "Spatial Distribution of Connexin43, the Major Cardiac Gap Junction Protein, in the Developing and Adult Rat Heart," *Circulation Research* 68, no. 6 (1991): 1638–1651.

52. K. Ronaldson-Bouchard, S. P. Ma, K. Yeager, et al., "Advanced Maturation of Human Cardiac Tissue Grown From Pluripotent Stem Cells," *Nature* 556, no. 7700 (2018): 239–243.

53. W. J. de Lange, E. T. Farrell, C. R. Kreitzer, et al., "Human iPSC-Engineered Cardiac Tissue Platform Faithfully Models Important Cardiac Physiology," *American Journal of Physiology-Heart and Circulatory Physiology* 320, no. 4 (2021): H1670–H1686.

54. K. S. Ginsburg and D. M. Bers, "Modulation of Excitation–Contraction Coupling by Isoproterenol in Cardiomyocytes With Controlled SR Ca^{2+} Load and Ca^{2+} Current Trigger," *The Journal of Physiology* 556, no. 2 (2004): 463–480.

55. J. Gromada, T. D. Jørgensen, and S. Dissing, "The Release of Intracellular Ca^{2+} in Lacrimal Acinar Cells by α-, β-Adrenergic and Muscarinic Cholinergic Stimulation: The Roles of Inositol Triphosphate and Cyclic

ADP-Ribose," *Pflügers Archiv—European Journal of Physiology* 429, no. 6 (1995): 751–761.

56. N. T. Feric and M. Radisic, "Maturing Human Pluripotent Stem Cell-Derived Cardiomyocytes in Human Engineered Cardiac Tissues," *Advanced Drug Delivery Reviews* 96 (2016): 110–134.

57. J.-L. Ruan, N. L. Tulloch, M. V. Razumova, et al., "Mechanical Stress Conditioning and Electrical Stimulation Promote Contractility and Force Maturation of Induced Pluripotent Stem Cell-Derived Human Cardiac Tissue," *Circulation* 134, no. 20 (2016): 1557–1567.

58. S. Israeli-Rosenberg, A. M. Manso, H. Okada, and R. S. Ross, "Integrins and Integrin-Associated Proteins in the Cardiac Myocyte," *Circulation Research* 114, no. 3 (2014): 572–586.

59. L. Miao, Y. Lu, A. Nusrat, et al., "B1 Integrins Regulate Cellular Behaviour and Cardiomyocyte Organization During Ventricular Wall Formation," *Cardiovascular Research* 120, no. 11 (2024): 1279–1294.

60. T. D. Ross, B. G. Coon, S. Yun, et al., "Integrins in Mechanotransduction," *Current Opinion in Cell Biology* 25, no. 5 (2013): 613–618.

61. J. Demmerle, A. J. Koch, and J. M. Holaska, "The Nuclear Envelope Protein Emerin Binds Directly to Histone Deacetylase $_3$ ($HDAC_3$) and Activates $HDAC_3$ Activity," *Journal of Biological Chemistry* 287, no. 26 (2012): 22080–22088.

62. S. Jiao, C. Li, F. Guo, et al., "SUN1/2 Controls Macrophage Polarization via Modulating Nuclear Size and Stiffness," *Nature Communications* 14, no. 1 (2023): 6416.

63. S.-J. Heo, S. D. Thorpe, T. P. Driscoll, R. L. Duncan, D. A. Lee, and R. L. Mauck, "Biophysical Regulation of Chromatin Architecture Instills a Mechanical Memory in Mesenchymal Stem Cells," *Scientific Reports* 5 (2015): 16895.

64. C. J. Walker, C. Crocini, D. Ramirez, et al., "Nuclear Mechanosensing Drives Chromatin Remodelling in Persistently Activated Fibroblasts," *Nature Biomedical Engineering* 5, no. 12 (2021): 1485–1499.

65. A. R. Killaars, J. C. Grim, C. J. Walker, E. A. Hushka, T. E. Brown, and K. S. Anseth, "Extended Exposure to Stiff Microenvironments Leads to Persistent Chromatin Remodeling in Human Mesenchymal Stem Cells," *Advanced Science* 6, no. 3 (2019): 1801483.

66. E. N. Dai, S. J. Heo, and R. L. Mauck, ""Looping In" Mechanics: Mechanobiologic Regulation of the Nucleus and the Epigenome," *Advanced Healthcare Materials* 9, no. 8 (2020): 2000030.

67. S. J. Seo and Y. Jin, "Enhancing Cardiomyocyte Purity Through Lactate-Based Metabolic Selection," *Tissue Engineering and Regenerative Medicine* 22, no. 2 (2025): 249–260.

68. E. Ehler, T. Moore-Morris, and S. Lange, "Isolation and Culture of Neonatal Mouse Cardiomyocytes," *Journal of Visualized Experiments*, no. 79 (2013): e50154.

69. B. J. van Meer, L. Sala, L. G. J. Tertoolen, G. L. Smith, F. L. Burton, and C. L. Mummery, "Quantification of Muscle Contraction In Vitro and In Vivo Using MUSCLEMOTION Software: From Stem Cell-Derived Cardiomyocytes to Zebrafish and Human Hearts," *Current Protocols in Human Genetics* 99, no. 1 (2018): 67.

70. K.-M. Koo, S. J. Seo, C.-D. Kim, et al., "In Situ Monitoring of Mitochondrial Redox Dynamics During Cardiac Reprogramming Using a Poly-L-Lysine/Matrigel-Coated Gold Nanostructured Composite Platform," *Advanced Composites and Hybrid Materials* 8, no. 3 (2025): 256.

Supporting Information

Additional supporting information can be found online in the Supporting Information section.

Supporting File: adfm74853-sup-0001-SuppMat.docx.

Supporting File: adfm74853-sup-0002-DataFile.xlsx.

Supporting File: adfm74853-sup-0002-MovieS1.mp4.

Supporting File: adfm74853-sup-0002-MovieS2.mp4.